





## 18 **Abstract**

19           As the major water resource in the southwestern United States, the Colorado River is  
20 experiencing decreases in naturalized streamflow and is predicted to face severe challenges  
21 under future climate scenarios. To better quantify these hydroclimatic changes, it is crucial that  
22 the scientific community establishes a reasonably accurate understanding of the spatial patterns  
23 associated with the basin hydrologic response. In this study, we employed remotely sensed Land  
24 Surface Temperature (LST) and Snow Cover Fraction (SCF) data from the Moderate Resolution  
25 Imaging Spectroradiometer (MODIS) to assess a regional hydrological model applied over the  
26 Colorado River Basin between 2003 and 2018. Based on the comparison between simulated and  
27 observed LST and SCF spatiotemporal patterns, a stepwise strategy was implemented to enhance  
28 the model performance. Specifically, we corrected the forcing temperature data, updated the  
29 time-varying vegetation parameters, and upgraded the snow-related process physics. Simulated  
30 nighttime LST errors were mainly controlled by the forcing temperature, while updated  
31 vegetation parameters reduced errors in daytime LST. Snow-related changes produced a good  
32 spatial representation of SCF that was consistent with MODIS but degraded the overall  
33 streamflow performance. This effort highlights the value of Earth observing satellites and  
34 provides a roadmap for building confidence in the spatiotemporal simulations from regional  
35 models for assessing the sensitivity of the Colorado River to climate change.

36  
37 **Keywords:** watershed hydrology; spatial patterns; surface energy balance; numerical modeling;  
38 Variable Infiltration Capacity model; southwestern United States.

39  
40



## 41 **1. Introduction**

42           Physically based numerical models of the coupled water-energy cycle have emerged as  
43 powerful tools to address critical societal needs (Fatichi et al., 2016), including flood forecasting  
44 (Maidment, 2017), irrigation operation (Gibson et al., 2017), weather and climate prediction  
45 (Baker et al., 2017; Senatore et al., 2015), and evaluations of water scarcity (Zhou et al., 2016).  
46 Over the last three decades, several types of hydrologic models have been developed with  
47 different levels of conceptualization that often change with the domain size due to computational  
48 constraints. One class of models, denoted as regional or macroscale models, were originally  
49 designed to serve as land surface scheme of atmospheric models and are routinely used to  
50 simulate hydrologic processes in continental basins ( $>10^5$  km<sup>2</sup>) at spatial resolutions of 10 to 25  
51 km (e.g., Lawrence et al., 2011; Liang et al., 1994; Niu et al., 2011). These processes include  
52 infiltration, evapotranspiration, runoff production, and snow accumulation and ablation, that are  
53 typically simulated in a regular grid without considering lateral transfers across cells (Clark et  
54 al., 2015). In recent years, the National Water Model combines a regional hydrologic model  
55 applied at the unprecedented resolution of 1 km with routing schemes to generate operational  
56 hydrologic predictions over the continental United States (Lahmers et al., 2019, 2021).

57           In many cases, hydrologic models are applied under prescribed meteorological forcings  
58 using an optimal set of parameters that are calibrated by minimizing differences between  
59 simulated streamflow and observations at one or more locations (e.g., Gou et al., 2021; Li et al.,  
60 2019; Nijssen et al., 1997; Xiao et al., 2018; Yun et al., 2020; Zhang et al., 2017). While widely  
61 used, this approach has two important limitations. First, input and structural uncertainties are  
62 often not taken into account (Gupta and Govindaraju, 2019), causing an inflation of parametric  
63 uncertainty that can exacerbate the problem of equifinality (Beven and Binley, 1992). Second,



64 this calibration method relies only on aggregated measure of the hydrologic response and does  
65 not consider the model ability to capture the spatially variable internal processes (Becker et al.,  
66 2019; K. Ajami et al., 2004). As a result of these two limitations, this calibration approach could  
67 cause the undesirable outcome that the model provides the right answer for the wrong physical  
68 reasons (Rajib et al., 2018; Tobin and Bennett, 2017), which can in turn induce wrong  
69 conclusions when the model is applied under nonstationary conditions due to changes in land  
70 cover and/or climate.

71 Satellite remote sensors provide spatially distributed estimates of hydrologic states and  
72 fluxes, including soil moisture (Entekhabi et al., 2010; Njoku et al., 2003; Kerr et al., 2001), land  
73 surface temperature (LST; Shi and Bates, 2011; Zhengming Wan and Dozier, 1996), snow cover  
74 fraction (SCF, Painter et al., 2009), evapotranspiration (Boschetti et al., 2019; Fisher et al.,  
75 2020), and changes in water storage (Tapley et al., 2004). These products can reduce parametric,  
76 structural, and input uncertainties of hydrologic models by including additional constraints in the  
77 calibration process (Wood et al., 2011; Fatichi et al., 2016; Ko et al., 2019). Despite this  
78 potential, the use of remote sensing products to reduce hydrologic simulation uncertainty has  
79 been explored in only a few studies. For instance, in studies by Corbari & Mancini (2014), Crow  
80 et al. (2003) and Zink et al. (2018), satellite LST was used with river discharge to calibrate  
81 model parameters, finding that including LST in the process improved the simulation of  
82 evapotranspiration as estimated by eddy covariance towers or other satellite products. This  
83 outcome was also found by Gutmann and Small (2010), who applied a regional model at 14 flux  
84 towers and showed that incorporating remotely-sensed LST estimates in the calibration allowed  
85 achieving two thirds of the improvements gained by ingesting more accurate ground LST data.  
86 In other efforts, satellite LST products have been used to verify performance of hydrologic



87 models, as done by Koch et al. (2016) with the North America Land Data Assimilation System  
88 (NLDAS), Xiang et al. (2014) with the TIN-based Real-time Integrated Basin Simulator (tRIBS),  
89 Xiang et al. (2017) with the Weather Research and Forecasting (WRF)-Hydro model, and Wang  
90 et al. (2021) with the Variable Infiltration Capacity (VIC) model. Finally, a few studies have  
91 enhanced streamflow simulations (Bennett et al., 2019; Bergeron et al., 2014; Tekeli et al., 2005)  
92 by improving the timing of snowmelt using remotely sensed snow cover fields.

93       The Colorado River Basin (CRB) is a regional watershed where hydrologic simulations  
94 are needed to support short- and long-term water management decisions. Its water resources are  
95 used by almost 40 million people in seven states of southwestern U.S. (Arizona, California,  
96 Colorado, Nevada, New Mexico, Utah, and Wyoming), to irrigate ~22,000 km<sup>2</sup> of land, and to  
97 generate over 4,200 MW of hydroelectric power (USBR, 2012). The mean annual discharge of  
98 the CRB is 20.2 km<sup>3</sup>, with high interannual variability resulting from large variations in climatic  
99 forcings (Christensen et al., 2004; Gautam and Mascaro, 2018). Until 2021, the CRB was able to  
100 meet the demand of all users by storing runoff in a large system of dams, mainly operated by the  
101 U.S. Bureau of Reclamation (USBR), and transporting water through canals and aqueducts,  
102 including the Central Arizona Project. However, declines in the mean flow observed over the last  
103 two decades (Hoerling et al., 2019; Udall and Overpeck, 2017) combined with increasing  
104 demands led to the first-ever declaration of water shortages in the CRB in January 2022. The  
105 water cuts affecting users in Arizona and Nevada (CAP, 2021) are expected to become more  
106 severe in the near future and impact the agricultural sector (Mitchell et al., 2022; Norton et al.,  
107 2021).

108       In previous studies on the hydrologic responses of the CRB using the VIC model,  
109 confidence in the model results was built mainly through comparisons against estimates of



110 naturalized flow (e.g., Christensen et al., 2004; Vano et al., 2012, 2014; Xiao et al., 2018). The  
111 CRB is characterized by a marked difference between the colder and wetter Upper Basin, where  
112 more than 90% of streamflow is generated (Li et al., 2017), and the warmer and drier Lower  
113 Basin with reduced runoff production due to low precipitation, high evaporative demand, and  
114 channel transmission losses (Rajagopalan et al., 2009). As a result of this large contrast, limiting  
115 the calibration of VIC to the use of naturalized flow in the Upper Basin may lead to uncertainty  
116 on its ability to simulate the spatiotemporal hydrologic response.

117         The objective of this study is to improve the physical reliability of VIC simulations in the  
118 CRB by incorporating remotely sensed fields of LST and SCF obtained from the Moderate  
119 Resolution Imaging Spectroradiometer (MODIS). LST is an important variable that impacts the  
120 coupled water-energy balance, while SCF provides information on snow conditions which are  
121 crucial to quantify runoff generation. We start from a parameterization of VIC that led to good  
122 estimates of monthly discharge in the period 2003-2018. We then apply a stepwise procedure to  
123 reduce uncertainties on model forcings, parameters, and structure based on comparisons of  
124 simulated and remotely sensed LST and SCF fields. While based on VIC, the methods proposed  
125 here can provide guidance to refine the calibration and reduce uncertainties of other physically  
126 based hydrologic models, as well as to identify areas for structural improvement.

127

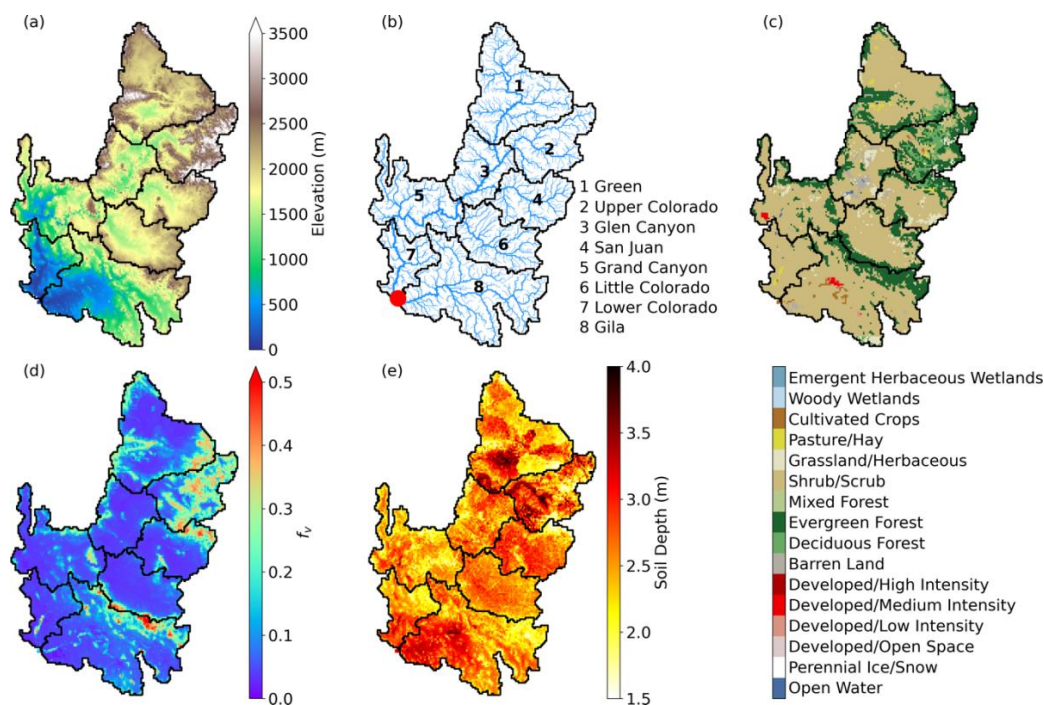
## 128 **2. Study Area and Datasets**

### 129 *2.1 Study basin*

130         The CRB has a total area of approximately 630,000 km<sup>2</sup>, covering seven states in United  
131 States and a small portion in Mexico. Here, we considered the drainage area above Imperial  
132 Dam, plus the Gila River (Fig. 1). The Colorado River Compact of 1922 divides the CRB into  
133 the Upper and Lower Basins. As revealed by the land cover map reported in Fig. 1c, most of the



134 basin is covered by shrub or scrub ecosystems (~60%), followed by various forest types (~24%).  
135 Table 1 summarizes the mean hydroclimatic and land surface features of the subbasins. The



136 **Figure 1.** (a) Digital elevation model of the CRB. (b) Channel network and eight subbasins  
137 analyzed in this study. The red circle marks Imperial Dam. (c) Dominant vegetation type in each  
138 pixel with legend. (d) Time-averaged vegetation fraction,  $f_v$ . (e) Total soil depth. All maps are at  
139 0.0625° (~6 km) spatial resolution. Values of  $f_v$  and soil depth are from the baseline simulation.

141  
142 Upper Basin consists of the Green, Upper Colorado, Glen Canyon, and San Juan River  
143 subbasins. These higher elevation subbasins (except Glen Canyon) receive more snowfall than  
144 the rest of the CRB, resulting in the presence of a significant snowpack (mean annual snow water  
145 equivalent, or SWE, ranges from 13.7 to 58.8 mm) that eventually leads to the generation of  
146 ~90% of the CRB runoff. While the Lower Basin receives about 60% of the mean annual



147 precipitation of the subbasins in the Upper Basin per unit area, its runoff ratio (i.e., the fraction  
148 of annual precipitation becoming runoff) is three times smaller than that of the Upper Basin.





	CRB	Green	Upper Colorado	San Juan	Glen Canyon	Little Colorado	Grand Canyon	Lower Colorado	Gila
<b><i>P</i> (mm yr<sup>-1</sup>)</b>	350.9	405.5	539	348.8	267.4	293.5	294.6	209.7	357.9
<b>SWE (mm)</b>	17.6	58.8	48.6	13.7	5.5	0.9	1.7	0.1	0.4
<b><i>Q</i> (mm yr<sup>-1</sup>)</b>	36.9	73.9	126.2	45.7	16.6	5.2	12.3	8.3	9.9
<b><i>Q/P</i> (%)</b>	10.5	18.2	23.4	13.1	6.2	1.8	4.2	4	2.8
<b>Area (10<sup>3</sup> km<sup>2</sup>)</b>	629.5	105.9	62.5	59.2	55.9	68.5	80	42	155.6
<b>Soil depth (m)</b>	2.55	2.55	2.69	2.62	2.52	2.55	2.36	2.48	2.6
<b>Elevation (m)</b>	1729.1	2215.3	2542.3	2034.3	1823.8	1929.3	1503.1	708.8	1184.6
<b>Percentage of trees (%)</b>	25.2	27.8	62	24.9	15.4	23.8	20.9	2.9	20.6

149  
 150  
 151  
 152

**Table 1.** Spatially averaged mean annual precipitation (*P*), snow water equivalent (SWE), runoff (*Q*), and runoff ratio (*Q/P*), along with area, mean elevation, mean soil depth, and percentage of trees in the CRB and its subbasins.



153 *2.2 Remote sensing and ground-based datasets*

154 We integrated different remotely sensed and ground-based data. Meteorological forcings  
155 were obtained from the gridded (0.0625° or ~6 km) daily datasets of Livneh et al. (2013) and Su  
156 et al. (2021) for precipitation, maximum temperature, minimum temperature, and wind speed.  
157 We also used the Precipitation Regression on Independent Slopes Method (PRISM) 30-year  
158 normal (Di Luzio et al., 2008) for temperature corrections. For assessing streamflow  
159 performance, we used monthly naturalized flow records from USBR at four interior locations of  
160 the Upper Basin. To improve the simulation of spatial patterns, we used two products from the  
161 Aqua MODIS sensor: daily LST (MYD11A1) and monthly SCF (MYD10CM). The LST product  
162 is available at 1-km resolution twice a day at about 1 p.m. (daytime) and 1 a.m. (nighttime) local  
163 times (Wan, 2013). The percent of missing data, largely due to cloud cover, varies from 42% to  
164 95% with larger values in the winter season and July (Fig. S1). Monthly SCF is provided at 0.05°  
165 (~5 km) resolution as the average of SCF for days with a prescribed level of sky clearness (Hall  
166 & Riggs, 2016). Both MODIS products were aggregated to the 0.0625° scale used in the model.  
167 We also validated simulated and remotely-sensed LST using measurements at 14 eddy  
168 covariance towers (Baldocchi et al., 2001) selected based on available data (>300 days over  
169 2003-2018). The station locations are shown in Fig. S2, with twelve located in the Lower Basin  
170 at elevations from 987 to 2618 m. Five stations were forested, and the remaining were covered  
171 by a short canopy. We extracted records of observed longwave radiation at the stations and used  
172 them to compute LST following Wang et al. (2021). We also used the National Land Cover  
173 Database (NLCD) Multi-Resolution Land Characteristics (MRLC) rangeland and tree canopy  
174 cover products, which contains canopy cover fraction at 30-m resolution for forests and  
175 shrublands (Coulston et al., 2012; Homer et al., 2020).

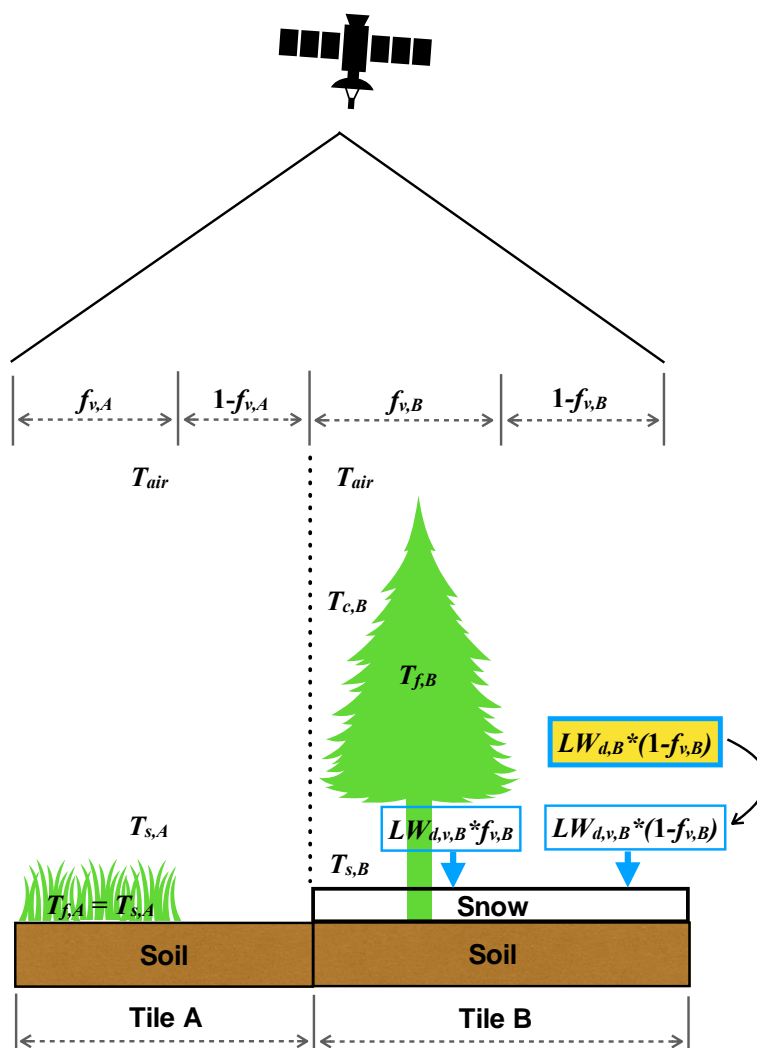


## 176 **3. Methods**

### 177 *3.1. The Variable Infiltration Capacity model*

178 We used the VIC model version 5.0 (Hamman et al., 2018) to simulate the hydrologic  
179 response of the CRB from 2003-2018 at an hourly time step and  $0.0625^\circ$  resolution. VIC is a  
180 macroscale, physically based model that solves the water and energy balance on a regular grid.  
181 Land surface heterogeneity in each cell is modeled through land cover tiles, each with a single  
182 vegetation class on top of a three-layer soil column. The model requires meteorological forcings  
183 as inputs and returns outputs over the grid. Fluxes and state variables simulated at grid cells are  
184 calculated as the areal weighted average of separate computations of the water and energy  
185 balances for each land cover tile. Here, we adopted the VIC version with the clumped vegetation  
186 scheme proposed by Bohn & Vivoni (2016), where the vegetation fraction ( $f_v$ ) accounts for  
187 spacing among plants in each tile. This modification allows simulating the energy balance with a  
188 higher fidelity, as shown by Bohn & Vivoni (2016) through the comparison with ground  
189 estimates of evapotranspiration in the southwestern U.S. and northwestern Mexico.

190 Since our adjustment strategy is based on the comparison of simulated and remotely  
191 sensed LST and SCF, we describe how these variables are simulated using the schematic in Fig.  
192 2. The governing equations are reported in Appendix A, while the most influential parameters  
193 are in Table 2. In our simulations, 16 vegetation classes are used, which include four types of tall  
194 trees: deciduous forest, evergreen forest, mixed forest, and woody wetlands. For other canopy  
195 types (e.g., tile A of Fig. 2), the energy balance is solved over a control volume that combines  
196 the fractions of vegetation ( $f_{v,A}$ ) and bare soil ( $1 - f_{v,A}$ ) using a weighted aerodynamic resistance.  
197 A single surface temperature ( $T_{s,A}$ ) is computed and assumed uniform over the tile and equal to  
198 the foliage temperature ( $T_{f,A} = T_{s,A}$ ). For tall trees (e.g., tile B in Fig. 2), a vegetated overstory and



199  
 200 **Figure 2.** Schematic explaining how LST is computed in VIC (LST<sub>v</sub>) as compared to MODIS  
 201 (LST<sub>m</sub>) in a pixel covered by short vegetation (tile A) and tall trees (tile B).  $f_v$  is the vegetation  
 202 fraction;  $T_{air}$  is the air temperature;  $T_s$ ,  $T_f$ , and  $T_c$  are simulated temperatures for the surface,  
 203 canopy, and canopy air;  $LW_{d,v}$  is the downward longwave radiation from the canopy; and  $LW_d$  is  
 204 the downward longwave radiation from the atmosphere. A and B refer to variables in each tile.  
 205



206 **Table 2.** List of spatially-variable forcings, vegetation and soil parameters, and state variables  
 207 involved in the computation of the energy balance (symbols defined in main text and Appendix  
 208 A). Forcings and state variables vary each hour. Parameters are either constant in time or vary  
 209 each month (denoted with <sup>+</sup>).

Energy balance component	Forcings	Vegetation parameters	Soil parameters	State variables
$R_n$	$R_s, R_L$	$\alpha^+, f_v^+$		$T_s$
$LH$	$R_s, R_L, T_{air},$ vapor pressure, wind speed	$LAI^+, r_{arc}, r_{min},$ $f_v^+$	$D_1$	$W, G_{sm}, T_s$
$SH$	$T_{air},$ wind speed	$z_0, d_0, f_v^+$		$T_s$
$GH$			$D_1$	$T_s, T_1$

210

211

212 an understory without vegetation are introduced. If snow is absent, the overstory foliage  
 213 temperature is assumed equal to air temperature ( $T_{f,B} = T_{air}$ ) and a single  $T_{s,B}$  in the understory is  
 214 calculated with the scheme described above. When snow is present,  $T_{s,B}$  is calculated by solving  
 215 the energy balance in the overstory, understory, and the atmosphere surrounding the canopy.  
 216 Since the satellite sensor observes the top of the surface, the simulated LST by VIC (LST<sub>V</sub>) that  
 217 is compared against MODIS (LST<sub>M</sub>) is the weighted average of foliage temperature in tiles with  
 218 tall trees and the ground temperature in other tiles. In the case of Fig. 2, this leads to:

$$219 \quad LST_V = \frac{A_A \cdot T_{s,A} + A_B [f_{v,B} \cdot T_{f,B} + (1 - f_{v,B}) \cdot T_{s,B}]}{A_A + A_B}, \quad (1)$$

220 where  $A_A$  and  $A_B$  are the areas of tiles A and B, respectively.

221 To compute SCF in the grid cells, VIC allows subdividing each tile into elevation bands  
 222 to capture changes in forcing temperature due to terrain heterogeneity. Elevation bands are the  
 223 same for all tiles in a grid cell and limited typically to three bands in total. Given the mean



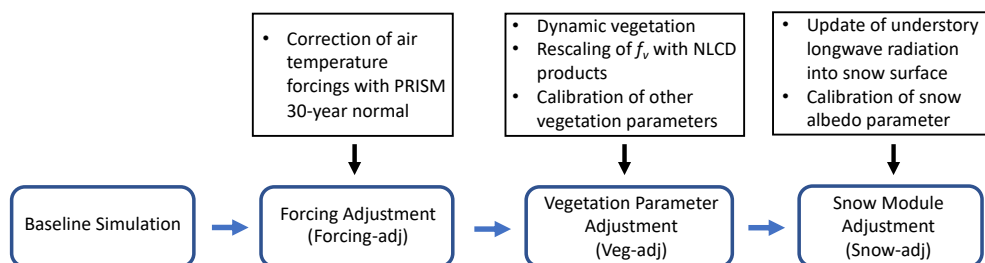
224 elevation of each elevation band, the air temperature forcing is adjusted using a lapse rate of -6.5  
225 °C/km and then used to solve the energy balance within each tile. Depending on temperature and  
226 precipitation, snow may be simulated within a tile and SWE is calculated. When  $SWE > 0$ , SCF  
227 is assumed to be 100%, such that a tile within that elevation band is fully covered with snow;  
228 otherwise, SCF is 0 and the elevation band within the tile is snow-free (i.e., a binary outcome).  
229 SCF in the grid cell is the area weighted average of the SCFs from all tiles and elevation bands.

### 230 *3.2. Baseline simulation*

231 We created a first model parameterization, labeled as “baseline”, based on applications  
232 by Xiao et al. (2018) and Bohn & Vivoni (2019). Hourly gridded meteorological forcings were  
233 generated from the daily grids of Livneh et al. (2013) and Su et al. (2021) using MetSim  
234 (Bennett et al., 2020; Bohn et al., 2013, 2019). Model parameters were obtained from Livneh et  
235 al. (2015), with a few updates as follows. Land surface parameters were based on MODIS and  
236 NLCD products from Bohn & Vivoni (2019), which include a land cover classification and  
237 climatological monthly means of leaf area index (LAI),  $f_v$ , and albedo. We replaced the elevation  
238 data used in prior VIC studies with the 30-m USGS National Elevation Dataset (USGS, 2016).  
239 The model was tested against monthly naturalized streamflow records by adjusting seven soil  
240 parameters that affect runoff production, as well as the parameters controlling the relation  
241 between snow albedo with snow age. As shown in Fig. S3, under the baseline simulation, VIC  
242 captured well the monthly streamflow in key subbasins of the Upper Basin where most runoff is  
243 produced and at the basin outlet, with a Nash-Sutcliffe efficiency (NSE)  $> 0.9$ .

### 244 *3.3. Model improvements with remote sensing products*

245 The baseline simulation was aimed at reproducing the streamflow response and did not  
246 consider the model ability to capture spatial patterns of hydrologic variables. We designed a



247  
248 **Figure 3.** Flowchart of the stepwise calibration procedure.  
249

250 stepwise strategy aimed at reducing the three main sources of uncertainty in the simulation of  
251 LST and SCF. A schematic of the procedure is reported in Fig. 3. In the first step (“Forcing-adj”  
252 or forcing adjustment), we targeted input uncertainty and modified air temperature to reduce  
253 errors of nighttime LST. In the second step (“Veg-adj” or vegetation adjustment), we focused on  
254 modifying spatially variable vegetation parameters affecting daytime LST identified among  
255 those reported in Table 2. The first two steps were guided by metrics quantifying the agreement  
256 between simulated and remotely sensed LST, including the correlation coefficient (CC), root  
257 mean squared error (RMSE), and Bias (mean  $LST_V$  - mean  $LST_M$ ) between: (1) time series of  
258 daily  $LST_V$  and  $LST_M$  at each grid cell, and (2) daily spatial maps. These metrics were obtained  
259 for both daytime and nighttime through comparisons at the MODIS overpass time.

260 After improving LST, we reduced structural uncertainty by modifying the computation of  
261 the snow energy balance in a step labeled as “Snow-adj” (or snow adjustment). As described  
262 above, when snow exists in tiles covered by tall trees, the downward longwave radiation into the  
263 understory (or ground) snowpack is assumed to originate from the overstory (indicated as  $LW_{d,v}$   
264 in Fig. 2, tile B). For areas without tall trees, the downward longwave radiation reaching the  
265 understory comes from the atmosphere (indicated as  $LW_d$ ). To account for this in the clumped  
266 canopy scheme, we modified the downward longwave radiation as the weighted average:  $[f_v \cdot$



267  $LW_{d,v} + (1 - f_v) \cdot LW_d]$ . In addition, we adjusted the empirical relation controlling the change  
268 of albedo during snow melt to reduce the Bias between VIC and MODIS SCF.

269

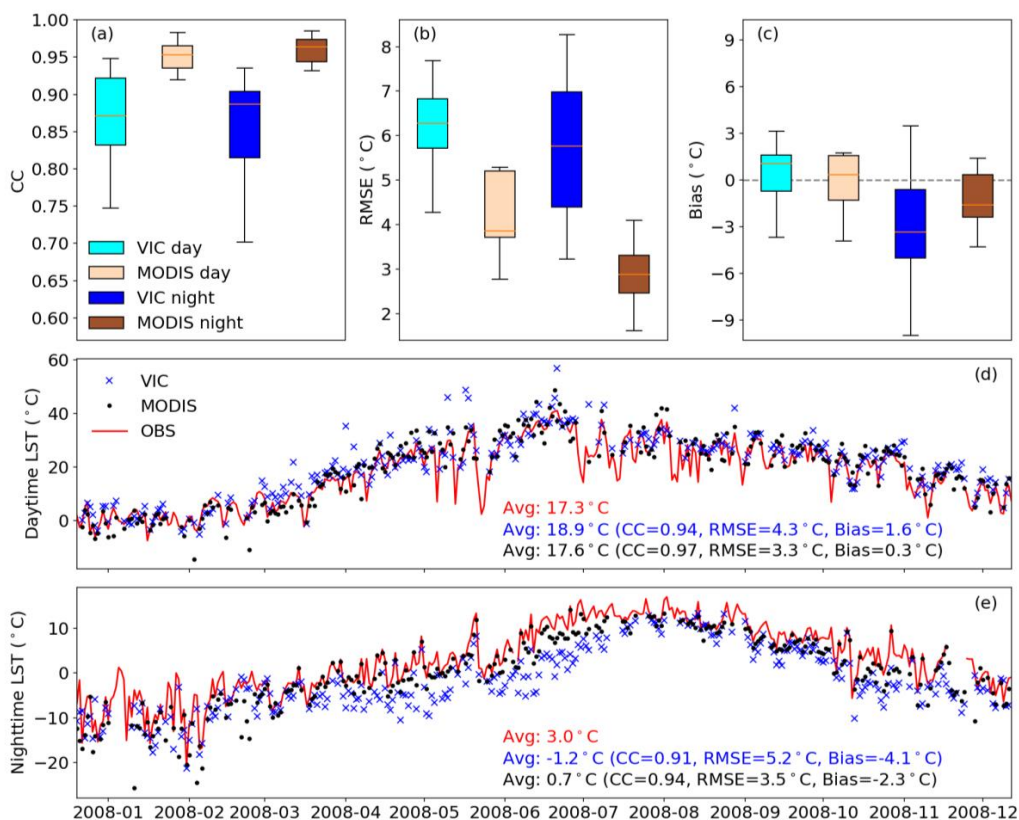
## 270 **4. Results**

### 271 *4.1. Comparison of VIC and MODIS LST with ground observations*

272 First, we provide an overview of the comparison among the time series of LST that were:  
273 (1) observed at the 14 eddy covariance stations, (2) simulated by VIC, and (3) retrieved from  
274 MODIS at the co-located 6-km pixel. The error metrics for the 14 stations are summarized  
275 through boxplots in Figs. 4a-c, while the time series of LST at a representative site for daytime  
276 and nighttime are shown in Figs. 4d-e. Station values and VIC simulations at the overpass times  
277 were extracted for comparison with MODIS. Dates with missing data in MODIS and station  
278 records were not considered. We find MODIS LST to be very strongly correlated with ground  
279 measurements ( $CC > 0.91$ ) and characterized by RMSE from  $\sim 1.5$  to  $5.3$  °C. Bias is slightly  
280 positive (negative) at daytime (nighttime) with a median of  $0.3$  °C ( $-1.6$  °C). The error metrics for  
281 VIC reveal that performance degrades moderately with larger variability across the stations: CC  
282 ranges from 0.70 to 0.95, the median RMSE is  $6.3$  °C ( $5.8$  °C) for daytime (nighttime), and the  
283 median Bias is  $1.1$  °C ( $-3.3$  °C) for daytime (nighttime). The error metrics against ground data  
284 provide a reference for evaluating the model improvements, as discussed next.

285





286

287

288 **Figure 4.** (a, b, c) Boxplots of CC, RMSE, and Bias comparing VIC and MODIS LST to

289 observations at 14 sites. Time series of daytime (d) and nighttime LST (e) at one site (Fuf

290 location shown in Fig. S2).

291

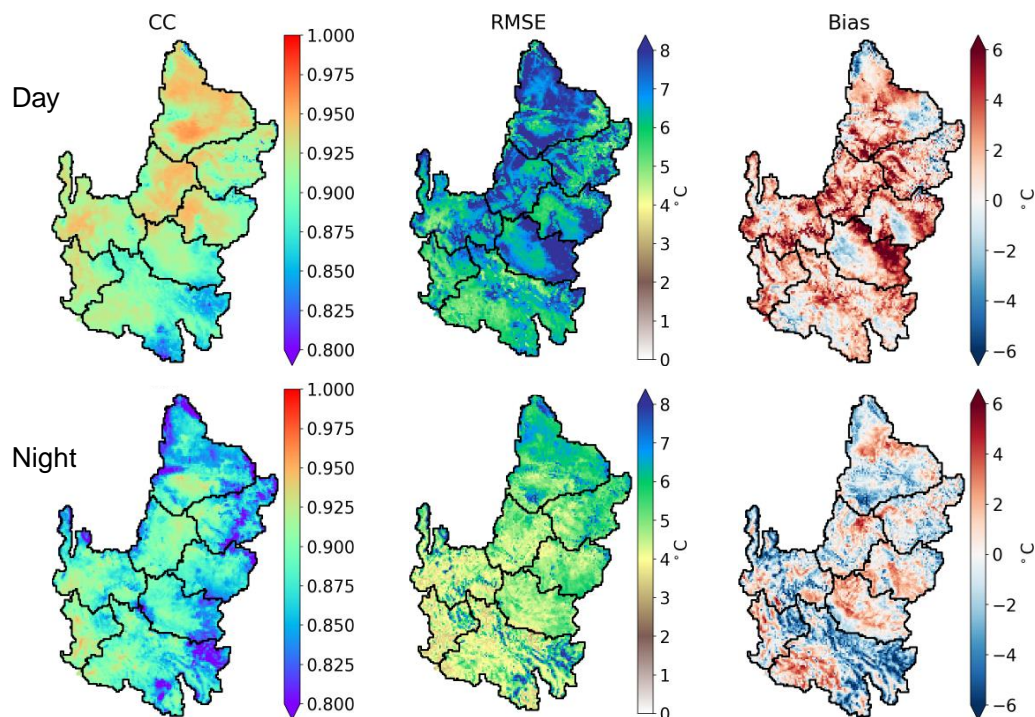
#### 292 4.2. Errors in the simulation of LST in the baseline simulation and their controls

293 Fig. 5 shows maps of CC, RMSE, and Bias of the time series of  $LST_V$  and  $LST_M$  at each

294 pixel for daytime and nighttime periods over the entire simulation from 2003 to 2018. To help

295 the interpretation, boxplots of the metrics in the grid cells within the CRB and three subbasins

296 are presented in Fig. 6. Results for other subbasins are reported in Figs. S4-S6 and Table S1.



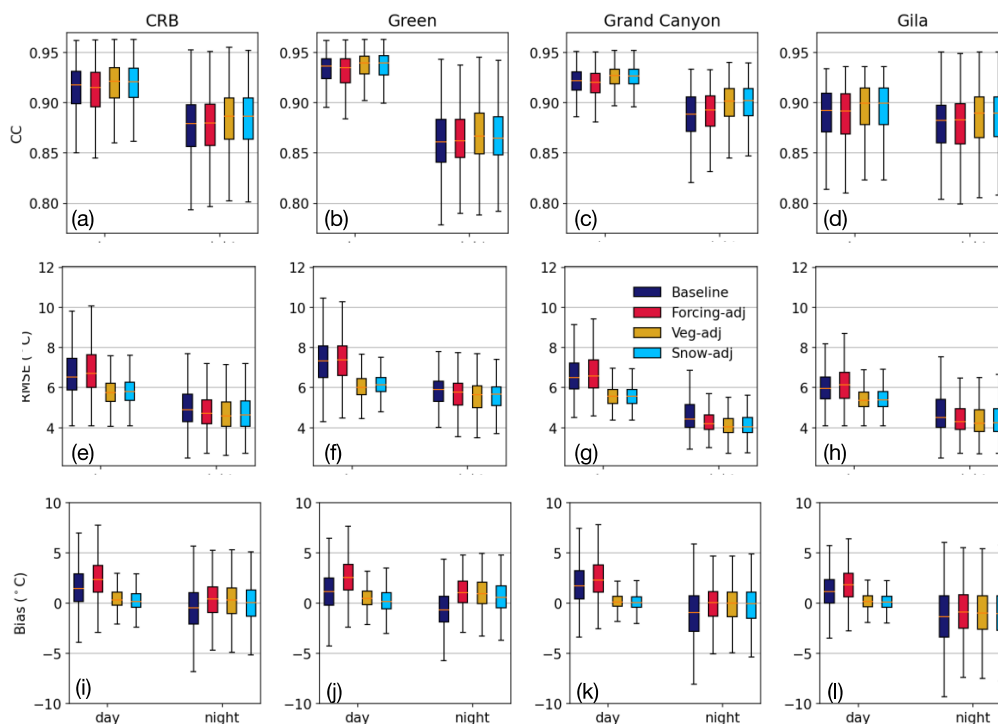
297

298

299 **Figure 5.** Spatial maps of CC, RMSE, and Bias between time series of LST<sub>v</sub> and LST<sub>m</sub> over

300 2003-2018 at each pixel. The top (bottom) row presents daytime (nighttime) comparisons.

301



302  
303

304 **Figure 6.** Boxplots of (a)-(d) CC, (e)-(h) RMSE, and (i)-(l) Bias between time series of LST<sub>v</sub>

305 and LST<sub>m</sub> in CRB pixels and three representative subbasins. Boxplots show median with 50%

306 and 90% confidence intervals. Different simulations are plotted in different colors.

307

308 Overall, CC is high (>0.8) throughout the CRB, with values like those found against station data.

309 CC is relatively higher for daytime than nighttime. On the other hand, RMSE maps show that

310 simulated LST matches better with MODIS during nighttime, with values largely consistent with

311 those found for stations. For both times of the day, RMSE is slightly larger in the Upper Basin.

312 Results for RMSE suggest that model performance for LST is relatively better at nighttime

313 without solar radiation forcing and tends to be better in drier and hotter regions in the Lower

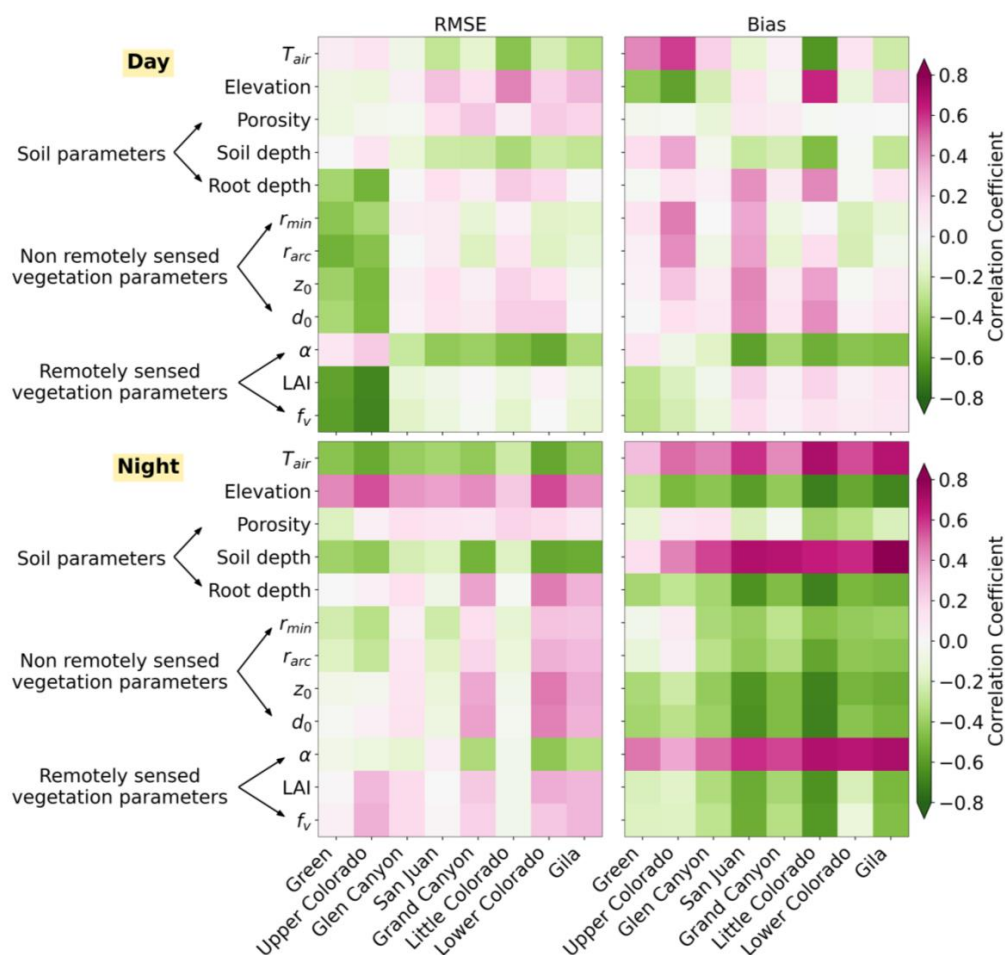
314 Basin. Bias maps reveal simulations of LST during daytime (nighttime) are warmer (cooler) than



315 MODIS observations in most of the CRB, with a median bias of 1.2 °C (-0.7 °C). These findings  
316 are largely consistent across the subbasins and with the station observations.

317 Spatial patterns of the metrics are complex, suggesting that LST simulation errors are  
318 impacted by several model parameters and forcings. To gain insights into these controls, we  
319 computed the correlation coefficient between the maps of error metrics and key parameters or  
320 forcings involved in the energy balance. Model parameter maps were created by calculating the  
321 area weighted averages within each grid cell. For monthly LAI, albedo, and  $f_v$ , we computed the  
322 annual mean map. For  $T_{air}$ , we calculated the mean across the entire study period. Figure 7  
323 summarizes the results in each subbasin for RMSE and Bias using heatmaps (also see Fig. S7 for  
324 CC). For daytime LST, the key factors change across the subbasins, while results are more  
325 spatially uniform for nighttime LST. During daytime, we found that the Green and Upper  
326 Colorado subbasins dominated by snow and evergreen forests exhibit different controls as  
327 compared to the other subbasins. Here, RMSE is highly correlated to  $f_v$  and LAI, while Bias is  
328 mainly controlled by  $T_{air}$ . In the other subbasins, albedo and, to a lesser extent,  $T_{air}$  are the  
329 dominant factors related to daytime RMSE. Different parameters affect the patterns of Bias,  
330 including albedo in all subbasins, most vegetation parameters, and root depth in the San Juan and  
331 Little Colorado, and  $T_{air}$  in the Little Colorado. Considering nighttime LST,  $T_{air}$  and, to a lower  
332 degree, soil depth are the main factors related to RMSE at all sites. Interestingly, nearly all  
333 parameters and  $T_{air}$  are linked to nighttime Bias. This is explained by considering that  $T_{air}$  is  
334 correlated with elevation and elevation is correlated with all other parameters (Fig. S8).

335



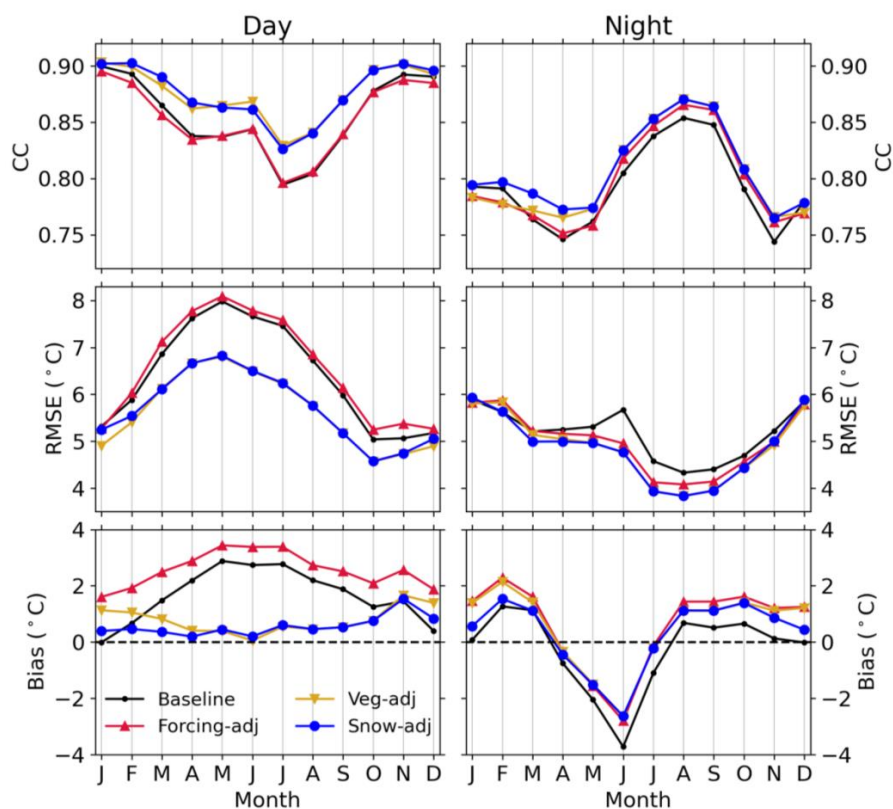
336  
 337 **Figure 7.** Heatmaps showing the correlation coefficient between (1)  $T_{air}$  or key soil and  
 338 vegetation parameters involved in the energy balance, and (2) the error metrics (left: RMSE,  
 339 right: Bias) between  $LST_M$  and  $LST_V$  at each subbasin for the baseline simulation. Symbols are  
 340 explained in Table 2. Top (bottom) row is for daytime (nighttime) LST.

341

342 Fig. 8 presents the intra-annual variability of the error metrics between daily pairs of  
 343  $LST_V$  vs.  $LST_M$  fields, shown as monthly averages. As found previously, CC is high for both  
 344 times of the day and relatively higher for daytime, while RMSE is larger at daytime. VIC



345 simulations at daytime are positively biased throughout the year, while Bias changes sign for  
 346 nighttime LST, being positive in winter and negative from April to July. In addition, both RMSE  
 347 and Bias of daytime LST are higher from April to July. This indicates that simulated daytime  
 348 LST degrades when incoming solar radiation is high, especially during snow-melting events after  
 349 peak SWE, typically around the end of March. To corroborate this, we repeated the analyses in  
 350 snow-dominated grid cells (mean annual maximum SWE > 30 mm) and for all other cells,  
 351 finding higher daytime RMSE in April for snow-dominated cells than other cells, indicating that  
 352 the LST during the ablation process is also more difficult to capture.



353  
 354  
 355 **Figure 8.** Time series of multiyear monthly average CC, RMSE, and Bias between VIC and  
 356 MODIS daily LST fields for the baseline simulation and each adjustment step.



357

358 *4.3. Stepwise reduction of uncertainty in the simulation of LST and SCF*

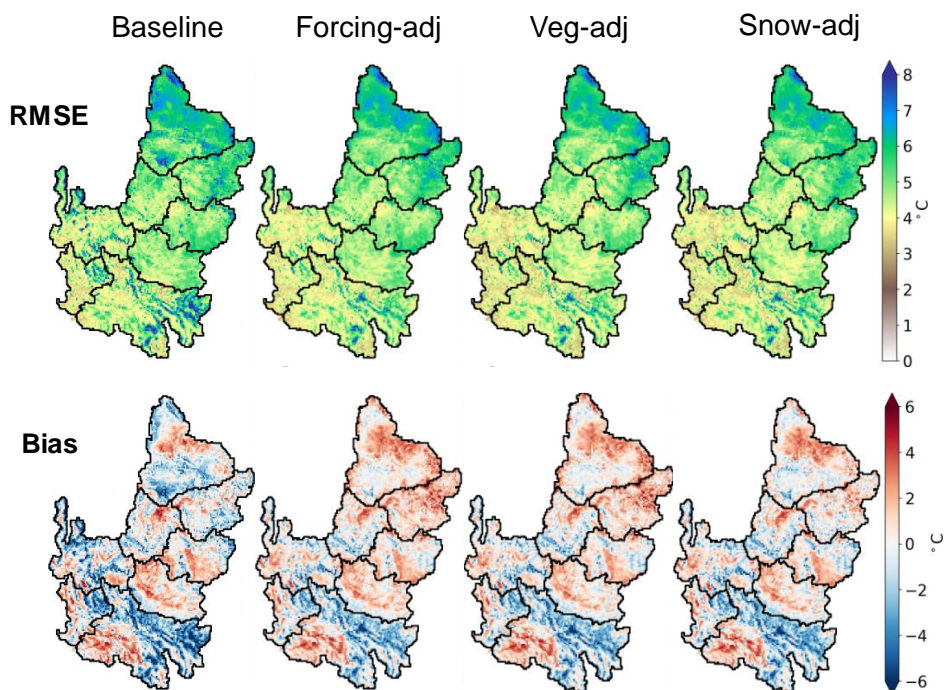
359 4.3.1. Forcing adjustment

360 We first focused on the improvement of simulated LST at nighttime. Fig. 7 indicates that  
361  $T_{air}$  is a key input affecting the energy balance at nighttime. Alder & Hostetler (2019) compared  
362 two air temperature datasets, finding that Livneh et al. (2013) products tend to be colder than  
363 PRISM in the mountain areas of the CRB. Based on this, we adjusted the daily minimum and  
364 maximum  $T_{air}$  in Livneh et al. (2013) and Su et al. (2021) to match the climatological (1981-  
365 2010) monthly means from PRISM. If  $T_{air,d,m}^L$  is the maximum or minimum daily  $T_{air}$  on day  $d$   
366 and month  $m$ , the bias-corrected value,  $T_{air,d,m}^{L,BC}$ , was obtained as:

$$367 \quad T_{air,d,m}^{L,BC} = T_{air,d,m}^L - (\bar{T}_{air,m}^P - \bar{T}_{air,m}^L), \quad (2)$$

368 where  $\bar{T}_{air,m}^P$  and  $\bar{T}_{air,m}^L$  are the climatological monthly means of maximum or minimum  $T_{air}$   
369 from PRISM and Livneh et al. (2013), respectively. Once we bias-corrected  $T_{air}$ , we regenerated  
370 the hourly forcings using MetSim. As shown in Fig. 9, the Forcing-adj simulations improved  
371 Bias, which was reduced in most subbasins. The nighttime RMSE also slightly decreased  
372 throughout the basin. These outcomes are reflected in the time series of Fig. 8 that also show that  
373 improvements (lower RMSE and Bias) occur largely in the warm season. On the other hand, the  
374 Forcing-adj simulations did not improve VIC performance at daytime, only yielding a slight  
375 increase of Bias (Figs. 6 and 8) that was fixed in the next steps.





376  
377 **Figure 9.** Spatial maps of the RMSE and Bias between time series of nighttime  $LST_v$  and  $LST_m$   
378 during 2003-2018 at each pixel for all steps. Top (bottom) row presents results of RMSE (Bias).  
379

#### 380 4.3.2. Vegetation parameter adjustment

381 Fig. 7 shows that both static and time-varying vegetation parameters affect the error  
382 metrics of LST. In the Veg-adj step, we modified a set of influential parameters by incorporating  
383 new datasets. We first replaced the climatological mean monthly values of LAI, albedo, and  $f_v$   
384 with yearly-varying monthly estimates from MODIS. Second, we updated  $f_v$  using new products  
385 from MRLC. In the baseline simulation,  $f_v$  was derived from Normalized Difference Vegetation  
386 Index (NDVI) retrieved from MODIS (Bohn and Vivoni, 2016, 2019). MRLC released 30-m





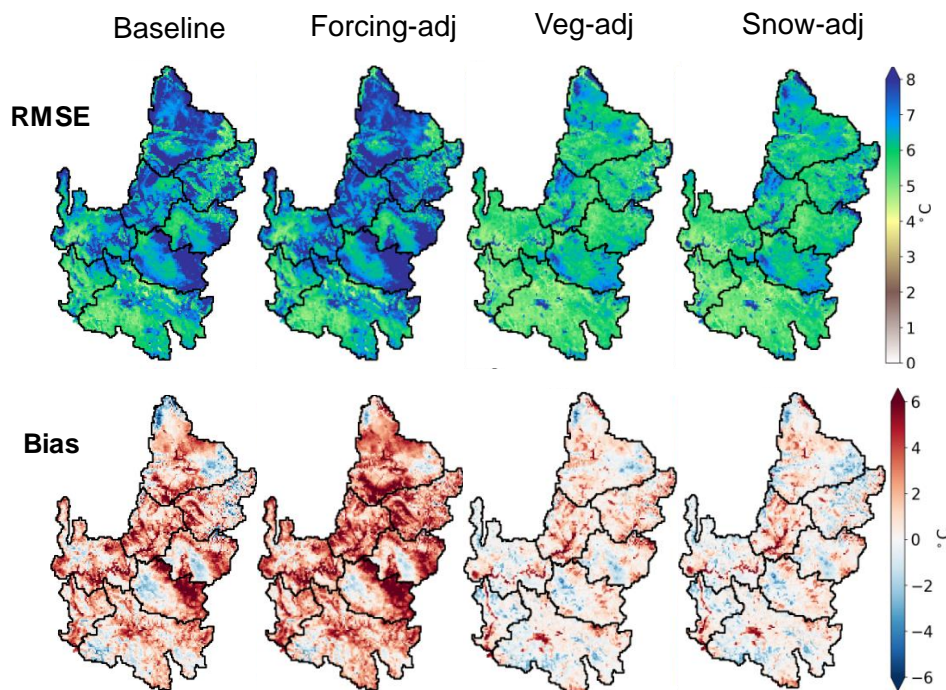
387 grids of mean annual  $f_v$  for major vegetation types in the CRB that were used to linearly rescale  
388 values of  $f_v$  in the shrub and trees classes to match the annual climatology of MRLC as:

$$389 \quad f_{v,m}^{Resc} = f_{v,m}^b \frac{\bar{f}_v^{MRLC}}{\bar{f}_v^b}, \quad (3)$$

390 where  $f_{v,m}^b$  is  $f_v$  in month  $m$  used in the baseline simulation,  $f_{v,m}^{Resc}$  is the rescaled value, and  
391  $\bar{f}_v^{MRLC}$  and  $\bar{f}_v^b$  are long-term mean annual values of MRLC and the baseline parameters.

392 Fig. 7 indicates that  $r_{min}$ ,  $r_{arc}$ ,  $d_o$ , and  $z_o$  affect errors in the simulation of LST, especially  
393 in the Green and Upper Colorado subbasins. Distributed estimates for these parameters are not  
394 currently available. Thus, we adjusted their values to reduce the Bias between daytime LST<sub>v</sub> and  
395 LST<sub>M</sub> guided by the process equations reported in Appendix A. Reducing  $z_o$  and  $d_o$  leads to  
396 lower aerodynamic resistance and higher sensible heat flux and, in turn, lower LST<sub>v</sub>. Increases in  
397  $r_{min}$  and  $r_{arc}$  lead to lower values of latent heat flux and higher LST<sub>v</sub>. Adjusting  $z_o$  has a greater  
398 impact than modifying the other parameter such that iteratively scaling of  $z_o$  in each pixel was  
399 performed at 25%, 50%, 150%, or 250% depending on the daytime LST Bias (Fig. 10). Changes  
400 were limited within physically plausible ranges. Next, we applied the same method to update  $d_o$ ,  
401  $r_{min}$ , and  $r_{arc}$ , but variations for these three parameters were minimal as documented in Fig. S9.

402 The Veg-adj simulation did not lead to significant changes of model performance at  
403 nighttime, confirming that the dominating factor affecting nighttime LST was  $T_{air}$ . On the other  
404 hand, improvements in the simulation of daytime LST were remarkable. Fig. 6 shows that both  
405 RMSE and Bias were reduced at all locations, both in terms of median ( $\sim 0.9$  °C) and variability  
406 in each subbasin (lower width of the confidence intervals), with values slightly higher than those  
407 found between MODIS and station observations (Fig. 4). These improvements were even more  
408 apparent in the maps of Fig. 10, which also showed that the complex spatial patterns of the errors  
409 of the baseline simulation have been replaced by more uniform and smoother patterns. The Veg-

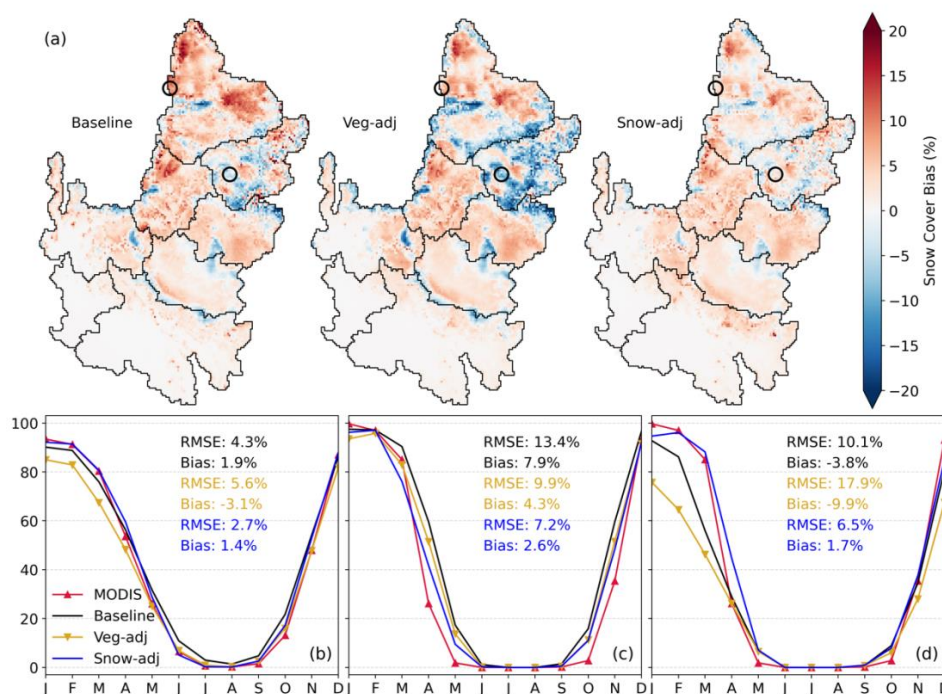


410  
411 **Figure 10.** Same as Figure 9 but for daytime LST.  
412

413 adj simulation also decreased large errors in the simulation of daytime LST from April to July,  
414 with lower RMSE, higher CC, and Bias close to 0 °C throughout the year (Fig. 8).

#### 415 4.3.3 Adjustment of snow dynamics

416 The Snow-adj step was aimed at improving the simulation of SCF. We first modified the  
417 computation of longwave radiation for tall trees which improved the simulation of SCF during  
418 the snow accumulation season. Next, a parameter of the relation controlling the decay of snow  
419 albedo was modified from 0.92 to 0.80, leading to an enhanced simulation of SCF in the ablation  
420 season. Fig. 11 presents Bias maps between simulated and observed mean monthly SCF and  
421 seasonality of SCF in snow-dominated cells for the baseline, Veg-adj, and Snow-adj simulations.  
422 Time series of SCF in two pixels are also shown to visualize differences in regions with positive



423  
 424

425 **Figure 11.** (a) Spatial maps of Bias between mean monthly SCF (VIC minus MODIS). Circles  
 426 indicate locations of two grid cells with positive and negative Bias. (b) Time series of multiyear  
 427 mean monthly SCF for snow-dominated cells. RMSE and Bias from monthly SCF comparisons  
 428 are reported. (c, d) Same as (b) but for site with positive and negative Bias, respectively.  
 429  
 430 and negative Bias. In the baseline simulation, SCF Bias was positive which occurs mainly during  
 431 May through October. Forcing corrections reduced SCF as  $T_{air}$  was increased in mountain areas.  
 432 Adjustments in the Snow-adj step reduced Bias in most locations during the accumulation and  
 433 ablation seasons. When averaged over time and in the CRB, SCF Bias was relatively small.  
 434 When focusing on single pixels, however, the Bias magnitude was larger, with differences in  
 435 seasonality depending on location. For example, Bias reached +20% in Fig. 11c from April to  
 436 December and -20% in Fig. 11d from November to March. As expected, Snow-adj changes



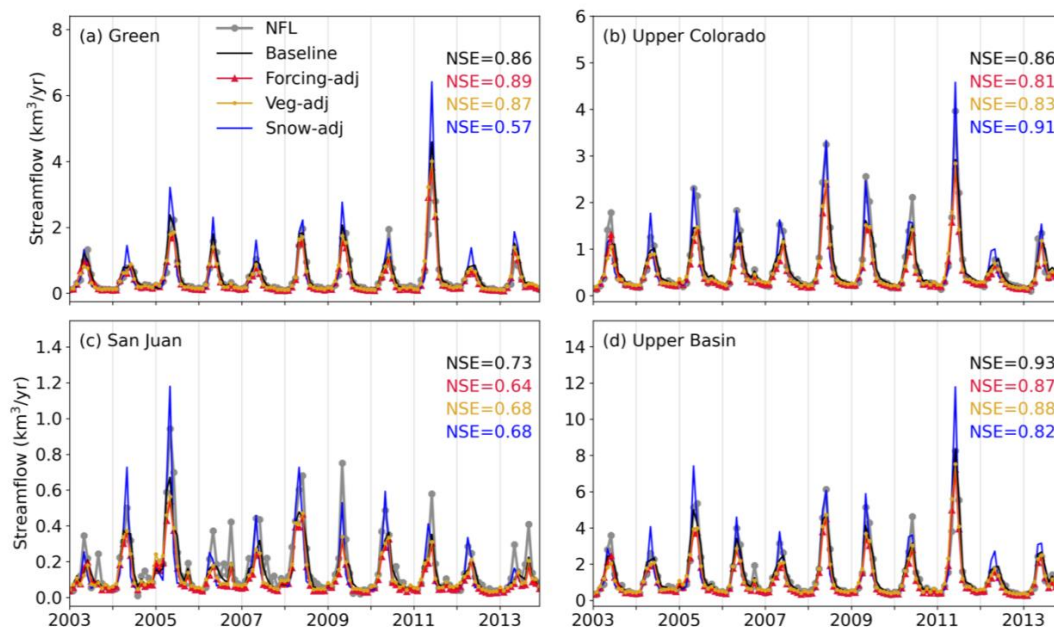
437 mainly impacted LST simulations in mountains, while a marginal influence occurred in the rest  
438 of the CRB. Overall, the daytime LST Bias map improved, while RMSE in mountain regions for  
439 both daytime and nighttime remained similar.

#### 440 *4.4. Impacts on VIC streamflow performance*

441 As shown previously (Corbari and Mancini, 2014; Crow et al., 2003), improving the  
442 simulation of hydrologic spatial patterns could affect streamflow performance since structural  
443 limitations and different degrees of conceptualization require further tuning. We investigated this  
444 in Fig. 12 using time series of monthly runoff in the Green and San Juan subbasins and the  
445 Upper Basin. Model performance is very good for baseline simulations since its calibration was  
446 tailored to naturalized streamflow records. Forcing and vegetation parameter adjustments slightly  
447 lowered performance (changes in  $NSE \leq 0.05$ ), whereas changes for the snow adjustment led to  
448 streamflow overestimation in May in all subbasins, especially in the Green subbasin ( $NSE$   
449 reduced to 0.57). Overall, simulated streamflow performance here is consistent with Tang and  
450 Lettenmaier (2010), who found that incorporating MODIS snow cover degrades streamflow  
451 metrics. We attribute this degradation in performance to a number of reasons. First, remotely  
452 sensed spatiotemporal data of SCF have limitations in its usefulness for tracking SWE which is  
453 the modeled state variable more directly impacting streamflow. Second, VIC uses a binary  
454 scheme for depicting SCF in elevation bands within each time of each grid cell, limiting its  
455 accuracy in representing topographic variations. To address these limitations, enhancements are  
456 needed in both simulation of snow physics and remote sensing of the spatial variation of snow  
457 depth or SWE at high spatiotemporal resolutions.

458

459



460

461

462

**Figure 12.** Monthly time-series of naturalized streamflow (NFL) and streamflow from baseline,

463

Forcing-adj, Veg-adj, and Snow-adj simulations at: (a) Green, (b) Upper Colorado, (c) San Juan,

464

and (d) Upper Basin for 2003-2013. NSE values are also reported.

465

## 466 5. Summary and Conclusions

467

In this study, we made improvement to a regional hydrologic model in the Colorado

468

River Basin using MODIS observations of land surface temperature and snow cover. Based on

469

the remotely sensed data, we corrected the meteorological forcings, updated the vegetation

470

parameters, and revised snow-related processes to enhance the model performance. The

471

adjustments increased the consistency between VIC and MODIS LST and SCF fields, thus

472

enhancing credibility of the spatial simulations. Our conclusions are summarized as follows:

473

1. MODIS products provided spatiotemporal information that can be used to identify

474

uncertainties in a hydrologic model calibrated with streamflow records at a few locations.



475 Although baseline simulation performance for LST was high (mostly  $CC > 0.8$ ), spatial errors  
476 within the CRB were non-negligible. The baseline simulation had lower RMSE of LST for  
477 nighttime and cold season conditions. Baseline model discrepancies were primarily associated  
478 with energy exchanges at land surface during periods of higher solar radiation.

479           2. Simulated nighttime LST values were dominated by the initial air temperature such  
480 that improvements were obtained from forcing corrections. This led to a reduction of nighttime  
481 LST Bias from  $-7$  to  $6$  °C in the baseline case to  $-5$  to  $5$  °C in the Forcing-adj simulation.

482 Vegetation adjustments led to large improvements in daytime LST, with RMSE reductions from  
483  $7.5$  °C to  $2.5$  °C but were less effective at night. In addition, the range of daytime RMSE of LST  
484 was reduced from  $4$  to  $10$  °C in the baseline case to  $2.5$  to  $3.5$  °C in the Veg-adj simulation.

485           3. Updated snow physics reduced the negative bias in SCF during the accumulation  
486 season. We further adjusted melting snow albedo to improve performance in the ablation period.  
487 Unlike other modifications, runoff was substantially impacted by the lower snow albedo. Thus,  
488 the consistency between VIC and MODIS snow cover did not ensure an improved streamflow  
489 simulation, demonstrating the limitations of the regional application in accurately capturing the  
490 variation of SWE in mountainous areas. A possible solution to improve the spatial credibility of  
491 the hydrologic model without degrading streamflow performance is by incorporating satellite  
492 products and ground observations into a multi-objective calibration.

493           Our work complements and expands efforts on validating physically based hydrologic  
494 simulations through remote sensing products. The adjustment steps led to the improvements of  
495 simulated LST that are in line with studies using hydrologic models with various levels of  
496 sophistication. For instance, simulations of Xiang et al. (2017) in a semiarid basin in northern  
497 Mexico found LST RMSE of  $4.3$  °C daytime and  $1.9$  °C at nighttime as compared to MODIS; the





498 hyperresolution (~80 m) simulations of Ko et al. (2019) in the same basin resulted in Bias of -  
499 1.4°C and CC of 0.87; and the high-resolution simulations with VIC in central Arizona by Wang  
500 et al. (2021) yielded LST biases between -1.5 and 3.6 °C. To our knowledge, this study is the  
501 first to improve the simulated spatial patterns of hydrologic variables in the CRB using remote  
502 sensing products. By increasing the credibility of the spatial model outputs, this effort builds  
503 confidence in using regional hydrologic models for water resources predictions and decision  
504 making under the on-going megadrought in the Colorado River.

## 505 **Acknowledgements**

506 This work was supported by NASA Earth Science Division Applied Science Program  
507 80NSSC19K1198: *Averting Drought Shortages in the Colorado River*. The authors declare no  
508 conflicts of interest, with respect to financial interests or to the results of this paper.

## 509 **Open Research**

510 MODIS products used in this study were retrieved from  
511 <https://modis.gsfc.nasa.gov/data/dataproduct/mod11.php> for LST and  
512 <https://modis.gsfc.nasa.gov/data/dataproduct/mod10.php> for SCF. Naturalized streamflow data is  
513 provided by USBR (<https://www.usbr.gov/lc/region/g4000/NaturalFlow/documentation.html>).  
514 MRLC land cover was extracted from <https://www.mrlc.gov/>. VIC parameters and source codes  
515 used in this study are archived at Zenodo (<https://doi.org/10.5281/zenodo.6565185>).

## 516 517 **Appendix A**

518 We describe the solution of the energy balance in VIC, which leads to the computation of  
519 ground surface temperature ( $T_s$ ) and canopy foliage temperature ( $T_f$ ) used to compute the land  
520 surface temperature variable,  $LST_v$ , that is compared against the MODIS estimate,  $LST_M$ . We



521 emphasize the main parameters and variables involved in the computation of these state  
522 variables. More detailed descriptions can be found in previous publications (Andreadis et al.,  
523 2009; Bohn & Vivoni, 2016; Cherkauer et al., 2003; Cherkauer & Lettenmaier, 1999; Liang et  
524 al., 1994). We first illustrate the original algorithm introduced in the first version of VIC (Liang  
525 et al., 1994), then the snow-overstory scheme introduced by Cherkauer & Lettenmaier (2003),  
526 and finally the clumped-canopy scheme implemented by Bohn & Vivoni (2016).

527 *Original scheme from Liang et al. (1994)*

528 In Liang et al. (1994), the minimal unit of simulation is the tile with a homogeneous land  
529 cover, i.e., the “big-leaf” approach. The energy balance equation for the tile can be expressed as:

$$530 \quad R_n = LH + SH + GH \quad , \quad (A1)$$

531 where  $R_n$  is net radiation,  $SH$  is sensible heat flux,  $LH$  is latent heat flux and  $GH$  is ground heat  
532 flux. The parameters and variables involved in the computation of each term are summarized in  
533 Table 2. Net radiation is determined by:

$$534 \quad R_n = (1 - \alpha) \cdot R_s + \varepsilon \cdot (R_L - \sigma \cdot T_s^4), \quad (A2)$$

535 where  $R_s$  and  $R_L$  are downward shortwave and longwave radiations,  $\alpha$  is albedo,  $\varepsilon$  is surface  
536 emissivity (0.98 for water; 0.97 for other conditions), and  $\sigma$  is the Stefan-Boltzmann constant.

537 The latent heat is computed as:

$$538 \quad LH = \rho_w \cdot \lambda_v \cdot (E_c + E_t + E_b), \quad (A3)$$

539 where  $\rho_w$  is the density of liquid water,  $\lambda_v$  is the latent heat of vaporization,  $E_c$  is evaporation  
540 from wet canopy,  $E_t$  is plant transpiration, and  $E_b$  is evaporation from surface soil moisture. For  
541 any given time, the maximum value of  $E_c$ , denoted as  $E_{c,max}$ , is calculated as:

$$542 \quad E_{c,max} = \left(\frac{W}{W_{max}}\right)^{2/3} \cdot E_p \cdot \left(\frac{r_a}{r_a + r_{arc}}\right), \quad (A4)$$





543 where  $W$  is the amount of canopy interception at a given time,  $W_{max}$  is the maximum amount of  
 544 water that the canopy can intercept (computed as  $0.2 \cdot LAI$ ),  $r_{arc}$  is the canopy architectural  
 545 resistance,  $r_a$  is the aerodynamic resistance,  $E_p$  is the potential evaporation derived from the  
 546 Penman-Monteith equation with a canopy resistance set to zero as:

$$547 \quad E_p = \frac{\Delta R_n + \rho_a \cdot c_p \cdot \delta e \cdot \frac{1}{r_a}}{[\Delta + \gamma \cdot (1 + \frac{r_s}{r_a})] \cdot \lambda_v}, \quad (A5)$$

548 where  $\Delta$  is the slope of the saturation vapor pressure temperature relationship,  $\rho_a$  is the air  
 549 density,  $c_p$  is the specific heat of air,  $\delta e$  is the vapor pressure deficit,  $\gamma$  is the psychrometric  
 550 constant, and  $r_s$  is the surface resistance. The aerodynamic resistance is calculated as:

$$551 \quad r_a = \frac{1}{C_w + u(z)}, \quad (A6)$$

552 where  $u(z)$  is the wind speed at the measurement height  $z$ , and  $C_w$  is the transfer coefficient for  
 553 water defined as:

$$554 \quad C_w = 1.351 \cdot \frac{k^2}{\left[ \ln \left( \frac{z - d_0}{z_0} \right) \right]^2} \cdot F(R_i), \quad (A7)$$

555 where  $k$  is the von Karman's constant,  $z_0$  is the roughness length,  $d_0$  is the displacement height,  
 556  $F(R_i)$  is a function of the Richardson number,  $R_i$ , that accounts for atmospheric stability.  $z_0$  and  $d_0$   
 557 have different values for each vegetation type and for bare soil and snow.  $R_i$  is defined as:

$$558 \quad R_i = \frac{g \cdot (T_{air} - T_s) \cdot z}{\left( \frac{T_{air} + T_s}{z} \right) \cdot u(z)^2}, \quad (A8)$$

559 where  $g$  is the gravitational acceleration, and  $T_{air}$  is the air temperature. When  $W \geq E_{c,max}$ ,  $E_c =$   
 560  $E_{c,max}$ ; otherwise,  $E_c$  is a fraction of  $E_{c,max}$  determined as a function of precipitation and  $W$ .

561 The transpiration,  $E_t$ , is calculated as:

$$562 \quad E_t = \left[ 1 - \left( \frac{W}{W_{max}} \right)^{\frac{2}{3}} \right] \cdot E_p \cdot \left( \frac{r_a}{r_a + r_{arc} + r_c} \right), \quad (A9)$$



563 where the canopy resistance,  $r_c$ , is related to the minimal stomatal resistance,  $r_{min}$ , via:

$$564 \quad r_c = r_{min} \cdot \frac{G_{sm}}{LAI} \quad . \quad (A10)$$

565  $G_{sm}$  is the soil moisture stress factor depending on root zone water availability (depth dependent  
566 on vegetation type). Bare soil evaporation,  $E_b$ , is equal to  $E_p$  when the shallowest soil layer is  
567 saturated; otherwise, it is computed as:

$$568 \quad E_b = E_p \cdot \left[ \int_0^{A_s} dA + \int_{A_s}^1 \frac{i_0}{i_m [1 - (1-A)^{1/b_i}]} dA \right], \quad (A11)$$

569 where  $A_s$  is the fraction of saturated soil, computed as (Zhao et al., 1980):

$$570 \quad A_s = 1 - \left( 1 - \frac{i_0}{i_m} \right)^{b_i}, \quad (A12)$$

571 where  $b_i$  is the infiltration shape parameter,  $i_0$  is the current infiltration capacity determined by  
572 water availability, and  $i_m$  is the maximum infiltration capacity computed as the product between  
573 maximum soil moisture (equal to soil depth times porosity) and  $(1 + b_i)$ .

574 The sensible heat flux,  $SH$ , is given by:

$$575 \quad SH = \frac{\rho_a \cdot c \cdot (T_s - T_{air})}{r_a}, \quad (A13)$$

576 where  $\rho_a$  and  $c$  are the mass density and specific heat of air at constant pressure, respectively.

577 The ground heat flux,  $GH$ , is calculated by:

$$578 \quad GH = \frac{\kappa}{D_1} (T_s - T_1), \quad (A14)$$

579 where  $T_1$  is soil temperature at depth  $D_1$  (0.1 m here) and  $\kappa$  is the soil thermal conductivity.

580 The equations described above are used to estimate  $T_s$  through an iterative procedure.  $T_s$   
581 is initially set to  $T_{air}$ , leading to  $R_i = 0$  and  $F(R_i) = 1$ ; evapotranspiration is then estimated and the  
582 energy balance is solved to update  $T_s$  (Liang et al., 1994). Iterative solutions for  $T_s$  are repeated  
583 until the difference between initial and final values are within a tolerance. This scheme is applied  
584 to the case of tile A in Fig. 2 when  $f_{v,A} = 1$ .



585

586

587 *Snow-overstory scheme from Cherkauer et al. (2003)*

588 The energy balance in VIC was improved with the snow-overstory scheme of Cherkauer  
589 et al. (2003). Andreadis et al. (2009) upgraded this scheme with fully-balanced energy terms and  
590 representation of snow interception. The scheme assumes a vegetated overstory (with foliage  
591 temperature  $T_f$ ) and an understory without vegetation (with surface temperature  $T_s$ ), as in tile B  
592 of Fig. 2 with  $f_{v,B} = 1$ . If snow is not present,  $T_f$  is assumed equal to  $T_{air}$  and  $T_s$  is calculated with  
593 the scheme described above. When snow is present, the energy balance is solved separately in  
594 control volumes (CVs) of the overstory, understory, and the atmosphere surrounding the canopy  
595 (with temperature  $T_c$ ), respectively. The algorithm involves the following steps:

596 1.  $T_c$  is initially assigned equal to  $T_{air}$ . The snow on the canopy is determined according to  
597 snowfall and maximum interception capacity,  $5e^{-4} \cdot L_r \cdot LAI$ , where  $L_r$  is a step function of  
598  $T_f$  from the last time step. If there is no snow on the trees,  $T_f = T_c = T_{air}$ . If there is snow on  
599 the trees and snow is melting,  $T_f = 0$  °C. If the snow is not melting, the energy balance of the  
600 overstory CV with snow is solved for  $T_f$ :

$$601 \quad R_n^{snow-canopy} + E_A = SH^{snow-canopy} + LH^{snow-canopy}, \quad (A15)$$

602 where  $E_A$  is energy advected by precipitation,  $SH^{snow-canopy}$  is calculated as in equation  
603 (A13) but with  $T_s$  and  $T_{air}$  replaced by  $T_f$  and  $T_c$ . The net radiation for snow on the canopy is:

$$604 \quad R_n^{snow-canopy} = (1 - \alpha_{snow}) \cdot R_s + \varepsilon \cdot (R_L + \sigma \cdot T_s^4 - 2 \cdot \sigma \cdot T_f^4), \quad (A16)$$

605 with  $\alpha_{snow}$  as the snow albedo. If  $T_s$  is not available, an initial value of 0 °C is used in  
606 equation (A16). The latent heat from snow sublimation is:

$$607 \quad LH^{snow-canopy} = \frac{0.622 \cdot \lambda_s \cdot \rho_a \cdot \delta e}{P_a \cdot r_{a,snow}}, \quad (A17)$$



608 where  $\lambda_s$  is the latent heat of sublimation,  $P_a$  is atmospheric pressure, and  $r_{a,snow}$  is the  
609 aerodynamic resistance near the snow surface.

610 2. The energy balance is then applied to the understory CV. Due to the presence of a tall tree,  
611 the shortwave radiation reaching the ground surface is reduced due to shading effect (by  
612 50%). The incoming longwave radiation is computed only as a function of  $T_f$ , while the  
613 contribution from the atmosphere is assumed negligible.  $T_s$  is then calculated by solving the  
614 energy balance. In this case, sensible heat is calculated using equation (A13) by replacing  $T_{air}$   
615 with  $T_c$ , and computing the aerodynamic resistance as:

$$616 \quad r_{a,snow} = \frac{\ln\left(\frac{z-d_s}{z_s}\right)^2}{k^2 \cdot u(z)}, \quad (A18)$$

617 where  $z_s$  is snow surface roughness and  $d_s$  is the snow depth. If there is no liquid water in the  
618 ground snowpack, the latent heat is calculated with equation (A17). If there is liquid water,  
619 equation (A17) is used with the latent heat of vaporization, i.e.,  $\lambda_s$  is replaced by  $\lambda_v$ .

620 3. Once  $T_s$  is derived,  $T_c$  is updated by solving the energy balance at the CV that includes the  
621 atmosphere surrounding the canopy:

$$622 \quad SH_{T_{air},T_c} = SH_{T_c,T_s} + SH_{T_c,T_f}, \quad (A19)$$

623 where  $SH_{T_c,T_s}$  is the sensible heat into snow calculated in step 2, and  $SH_{T_c,T_f}$  is the  
624  $SH^{snow-canopy}$  calculated in step 1.  $T_c$  is compared with its estimate from the previous step  
625 ( $T_{air}$  in first iteration). If the values are not included within a tolerance, steps 1-3 are repeated.

#### 626 *Clumped-canopy scheme from Bohn & Vivoni (2016)*

627 The schemes described above are based on the “big-leaf” approach, where vegetation was  
628 assumed to cover the entire surface of the tile. Bohn & Vivoni (2016) introduced the “clumped-  
629 canopy” scheme to improve the simulation of bare soil evaporation from inter-canopy spaces.



630 This scheme relies on the vegetation fraction ( $f_v$ ). The aerodynamic resistance of each tile is  
631 updated to be the inverse of aerodynamic conductance,  $1/g_a$ , with:

$$632 \quad g_a = (1 - f_v) \cdot 1/r_{a,s} + f_v \cdot 1/r_{a,v} \quad , \quad (A20)$$

633 where  $r_{a,s}$  and  $r_{a,v}$  are aerodynamic resistances for bare soil and vegetated area, respectively,  
634 computed using equation (A6). For the soil, a constant roughness height of 0.0001 m is used.

635 Because of the introduction of  $f_v$ , we improved the snow physics in the Snow-adj step.  
636 The version of VIC employed in our baseline simulation assumed that longwave radiation into  
637 the snowpack was received only from the canopy in the tiles covered by trees, even for the  
638 unvegetated fraction. In the clumped scheme, where a fraction  $(1 - f_v)$  is unvegetated, this  
639 assumption is not reliable. Therefore, we updated the computation of the longwave radiation as  
640 the weighted average of canopy longwave and longwave from atmosphere [ $LW_{d,v,B} \cdot (1 - f_{v,B})$  was  
641 replaced by  $LW_{d,B} \cdot (1 - f_{v,B})$  as highlighted in Fig. 2b].

642



643 **References**

- 644 Alder, J. R. and Hostetler, S. W.: The Dependence of Hydroclimate Projections in Snow-  
645 Dominated Regions of the Western United States on the Choice of Statistically Downscaled  
646 Climate Data, *Water Resour. Res.*, 55(3), 2279–2300, doi:10.1029/2018WR023458, 2019.
- 647 Andreadis, K. M., Storck, P. and Lettenmaier, D. P.: Modeling snow accumulation and ablation  
648 processes in forested environments, *Water Resour. Res.*, 45(5), 1–13,  
649 doi:10.1029/2008WR007042, 2009.
- 650 Baker, I. T., Sellers, P. J., Denning, A. S., Medina, I., Kraus, P., Haynes, K. D. and Biraud, S. C.:  
651 Closing the scale gap between land surface parameterizations and GCMs with a new scheme,  
652 SiB3-Bins, *J. Adv. Model. Earth Syst.*, 9(1), 691–711, doi:10.1002/2016MS000764, 2017.
- 653 Baldocchi, D., Falge, E., Gu, L., Olson, R., Hollinger, D., Running, S., Anthoni, P., Bernhofer,  
654 C., Davis, K., Evans, R., Fuentes, J., Goldstein, A., Katul, G., Law, B., Lee, X., Malhi, Y.,  
655 Meyers, T., Munger, W., Oechel, W., Paw, U. K. T., Pilegaard, K., Schmid, H. P., Valentini, R.,  
656 Verma, S., Vesala, T., Wilson, K. and Wofsy, S.: FLUXNET: A New Tool to Study the  
657 Temporal and Spatial Variability of Ecosystem-Scale Carbon Dioxide, Water Vapor, and Energy  
658 Flux Densities, *Bull. Am. Meteorol. Soc.*, 82(11), 2415–2434, doi:10.1175/1520-  
659 0477(2001)082<2415:FANTTS>2.3.CO;2, 2001.
- 660 Becker, R., Koppa, A., Schulz, S., Usman, M., aus der Beek, T. and Schüth, C.: Spatially  
661 distributed model calibration of a highly managed hydrological system using remote sensing-  
662 derived ET data, *J. Hydrol.*, 577(June), 123944, doi:10.1016/j.jhydrol.2019.123944, 2019.
- 663 Bennett, A., Hamman, J. and Nijssen, B.: MetSim: A Python package for estimation and  
664 disaggregation of meteorological data, *J. Open Source Softw.*, 5(47), 2042,  
665 doi:10.21105/joss.02042, 2020.
- 666 Bennett, K. E., Cherry, J. E., Balk, B. and Lindsey, S.: Using MODIS estimates of fractional



667 snow cover area to improve streamflow forecasts in interior Alaska, *Hydrol. Earth Syst. Sci.*,  
668 23(5), 2439–2459, doi:10.5194/hess-23-2439-2019, 2019.

669 Bergeron, J., Royer, A., Turcotte, R. and Roy, A.: Snow cover estimation using blended MODIS  
670 and AMSR-E data for improved watershed-scale spring streamflow simulation in Quebec,  
671 Canada, *Hydrol. Process.*, 28(16), 4626–4639, doi:10.1002/hyp.10123, 2014.

672 Beven, K. and Binley, A.: The future of distributed models: Model calibration and uncertainty  
673 prediction, *Hydrol. Process.*, 6(3), 279–298, doi:10.1002/hyp.3360060305, 1992.

674 Bohn, T. J. and Vivoni, E. R.: Process-based characterization of evapotranspiration sources over  
675 the North American monsoon region, *Water Resour. Res.*, 52(1), 358–384,  
676 doi:10.1002/2015WR017934, 2016.

677 Bohn, T. J. and Vivoni, E. R.: MOD-LSP, MODIS-based parameters for hydrologic modeling of  
678 North American land cover change, *Sci. Data*, 6(1), 1–13, doi:10.1038/s41597-019-0150-2,  
679 2019.

680 Bohn, T. J., Livneh, B., Oyster, J. W., Running, S. W., Nijssen, B. and Lettenmaier, D. P.: Global  
681 evaluation of MTCLIM and related algorithms for forcing of ecological and hydrological  
682 models, *Agric. For. Meteorol.*, 176, 38–49, doi:10.1016/j.agrformet.2013.03.003, 2013.

683 Boschetti, L., Roy, D. P., Giglio, L., Huang, H., Zubkova, M. and Humber, M. L.: Global  
684 validation of the collection 6 MODIS burned area product, *Remote Sens. Environ.*, 235, 111490,  
685 doi:10.1016/j.rse.2019.111490, 2019.

686 Cherkauer, K. A. and Lettenmaier, D. P.: Hydrologic effects of frozen soils in the upper  
687 Mississippi River basin, *J. Geophys. Res. Atmos.*, 104(D16), 19599–19610,  
688 doi:10.1029/1999JD900337, 1999.

689 Cherkauer, K. A. and Lettenmaier, D. P.: Simulation of spatial variability in snow and frozen



690 soil, *J. Geophys. Res. Atmos.*, 108(22), 1–14, doi:10.1029/2003jd003575, 2003.

691 Cherkauer, K. A., Bowling, L. C. and Lettenmaier, D. P.: Variable infiltration capacity cold land  
692 process model updates, *Glob. Planet. Change*, 38(1–2), 151–159, doi:10.1016/S0921-  
693 8181(03)00025-0, 2003.

694 Christensen, N. S., Wood, A. W., Voisin, N., Lettenmaier, D. P. and Palmer, R. N.: The effects  
695 of climate change on the hydrology and water resources of the Colorado River basin, *Clim.*  
696 *Change*, 62(1–3), 337–363, doi:10.1023/B:CLIM.0000013684.13621.1f, 2004.

697 Clark, M. P., Fan, Y., Lawrence, D. M., Adam, J. C., Bolster, D., Gochis, D. J., Hooper, R. P.,  
698 Kumar, M., Leung, L. R., Mackay, D. S. and Maxwell, R. M.: Hydrological partitioning in the  
699 critical zone: Recent advances and opportunities for developing transferable understanding of  
700 water cycle dynamics, *Water Resour. Res.*, 1–28, doi:10.1002/2015WR017096. Received, 2015.

701 Corbari, C. and Mancini, M.: Calibration and validation of a distributed energy-water balance  
702 model using satellite data of land surface temperature and ground discharge measurements, *J.*  
703 *Hydrometeorol.*, 15(1), 376–392, doi:10.1175/JHM-D-12-0173.1, 2014.

704 Crow, W. T., Wood, E. F. and Pan, M.: Multiobjective calibration of land surface model  
705 evapotranspiration predictions using streamflow observations and spaceborne surface  
706 radiometric temperature retrievals, *J. Geophys. Res. Atmos.*, 108(23), 1–12,  
707 doi:10.1029/2002jd003292, 2003.

708 Entekhabi, D., Njoku, E. G., O’Neill, P. E., Kellogg, K. H., Crow, W. T., Edelstein, W. N.,  
709 Entin, J. K., Goodman, S. D., Jackson, T. J., Johnson, J., Kimball, J., Piepmeier, J. R., Koster, R.  
710 D., Martin, N., McDonald, K. C., Moghaddam, M., Moran, S., Reichle, R., Shi, J. C., Spencer,  
711 M. W., Thurman, S. W., Tsang, L. and Van Zyl, J.: The Soil Moisture Active Passive (SMAP)  
712 Mission, *Proc. IEEE*, 98(5), 704–716, doi:10.1109/JPROC.2010.2043918, 2010.





713 Fatichi, S., Vivoni, E. R., Ogden, F. L., Ivanov, V. Y., Mirus, B., Gochis, D., Downer, C. W.,  
714 Camporese, M., Davison, J. H., Ebel, B., Jones, N., Kim, J., Mascaro, G., Niswonger, R.,  
715 Restrepo, P., Rigon, R., Shen, C., Sulis, M. and Tarboton, D.: An overview of current  
716 applications, challenges, and future trends in distributed process-based models in hydrology, *J.*  
717 *Hydrol.*, 537, 45–60, doi:10.1016/j.jhydrol.2016.03.026, 2016.

718 Fisher, J. B., Lee, B., Purdy, A. J., Halverson, G. H., Dohlen, M. B., Cawse-Nicholson, K.,  
719 Wang, A., Anderson, R. G., Aragon, B., Arain, M. A., Baldocchi, D. D., Baker, J. M., Barral, H.,  
720 Bernacchi, C. J., Bernhofer, C., Biraud, S. C., Bohrer, G., Brunsell, N., Cappelare, B., Castro-  
721 Contreras, S., Chun, J., Conrad, B. J., Cremonese, E., Demarty, J., Desai, A. R., De Ligne, A.,  
722 Foltýnová, L., Goulden, M. L., Griffis, T. J., Grünwald, T., Johnson, M. S., Kang, M., Kelbe, D.,  
723 Kowalska, N., Lim, J., Maïnassara, I., McCabe, M. F., Missik, J. E. C., Mohanty, B. P., Moore,  
724 C. E., Morillas, L., Morrison, R., Munger, J. W., Posse, G., Richardson, A. D., Russell, E. S.,  
725 Ryu, Y., Sanchez-Azofeifa, A., Schmidt, M., Schwartz, E., Sharp, I., Šigut, L., Tang, Y., Hulley,  
726 G., Anderson, M., Hain, C., French, A., Wood, E. and Hook, S.: ECOSTRESS: NASA’s Next  
727 Generation Mission to Measure Evapotranspiration From the International Space Station, *Water*  
728 *Resour. Res.*, 56(4), doi:10.1029/2019WR026058, 2020.

729 Gautam, J. and Mascaro, G.: Evaluation of Coupled Model Intercomparison Project Phase 5  
730 historical simulations in the Colorado River basin, *Int. J. Climatol.*, 38(10), 3861–3877,  
731 doi:10.1002/joc.5540, 2018.

732 Gibson, J., Franz, T. E., Wang, T., Gates, J., Grassini, P., Yang, H. and Eisenhauer, D.: A case  
733 study of field-scale maize irrigation patterns in western Nebraska: implications for water  
734 managers and recommendations for hyper-resolution land surface modeling, *Hydrol. Earth Syst.*  
735 *Sci.*, 21(2), 1051–1062, doi:10.5194/hess-21-1051-2017, 2017.



- 736 Gou, J., Miao, C., Wu, J., Guo, X., Samaniego, L. and Xiao, M.: CNRD v1.0: A High-Quality  
737 Natural Runoff Dataset for Hydrological and Climate Studies in China, *Bull. Am. Meteorol.*  
738 *Soc.*, 102(5), E929–E947, doi:10.1175/BAMS-D-20-0094.1, 2021.
- 739 Gupta, A. and Govindaraju, R. S.: Propagation of structural uncertainty in watershed hydrologic  
740 models, *J. Hydrol.*, 575(May), 66–81, doi:10.1016/j.jhydrol.2019.05.026, 2019.
- 741 Gutmann, E. D. and Small, E. E.: A method for the determination of the hydraulic properties of  
742 soil from MODIS surface temperature for use in land-surface models, *Water Resour. Res.*, 46(6),  
743 doi:10.1029/2009WR008203, 2010.
- 744 Hamman, J. J., Nijssen, B., Bohn, T. J., Gergel, D. R. and Mao, Y.: The variable infiltration  
745 capacity model version 5 (VIC-5): Infrastructure improvements for new applications and  
746 reproducibility, *Geosci. Model Dev.*, 11(8), 3481–3496, doi:10.5194/gmd-11-3481-2018, 2018.
- 747 Hoerling, M., Barsugli, J., Livneh, B., Eischeid, J., Quan, X. and Badger, A.: Causes for the  
748 Century-Long Decline in Colorado River Flow, *J. Clim.*, 8181–8203, doi:10.1175/jcli-d-19-  
749 0207.1, 2019.
- 750 Homer, C., Dewitz, J., Jin, S., Xian, G., Costello, C., Danielson, P., Gass, L., Funk, M.,  
751 Wickham, J., Stehman, S., Auch, R. and Riitters, K.: Conterminous United States land cover  
752 change patterns 2001–2016 from the 2016 National Land Cover Database, *ISPRS J.*  
753 *Photogramm. Remote Sens.*, 162(March), 184–199, doi:10.1016/j.isprsjprs.2020.02.019, 2020.
- 754 K. Ajami, N., Gupta, H., Wagener, T. and Sorooshian, S.: Calibration of a semi-distributed  
755 hydrologic model for streamflow estimation along a river system, *J. Hydrol.*, 298(1–4), 112–135,  
756 doi:10.1016/j.jhydrol.2004.03.033, 2004.
- 757 Ko, A., Mascaro, G. and Vivoni, E. R.: Strategies to Improve and Evaluate Physics-Based  
758 Hyperresolution Hydrologic Simulations at Regional Basin Scales, *Water Resour. Res.*, (88 m),



759 1–24, doi:10.1029/2018WR023521, 2019.

760 Koch, J., Siemann, A., Stisen, S. and Sheffield, J.: Spatial validation of large-scale land surface  
761 models against monthly land surface temperature patterns using innovative performance metrics,  
762 J. Geophys. Res. Atmos., 121(10), 5430–5452, doi:10.1002/2015JD024482, 2016.

763 Lahmers, T. M., Gupta, H., Castro, C. L., Gochis, D. J., Yates, D., Dugger, A., Goodrich, D. and  
764 Hazenberg, P.: Enhancing the structure of the WRF-hydro hydrologic model for semiarid  
765 environments, J. Hydrometeorol., 20(4), 691–714, doi:10.1175/JHM-D-18-0064.1, 2019.

766 Lahmers, T. M., Hazenberg, P., Gupta, H., Castro, C., Gochis, D., Dugger, A., Yates, D., Read,  
767 L., Karsten, L. and Wang, Y.-H.: Evaluation of NOAA National Water Model Parameter  
768 Calibration in Semi-Arid Environments Prone to Channel Infiltration, J. Hydrometeorol., (2019),  
769 2939–2970, doi:10.1175/jhm-d-20-0198.1, 2021.

770 Lawrence, D. M., Oleson, K. W., Flanner, M. G., Thornton, P. E., Swenson, S. C., Lawrence, P.  
771 J., Zeng, X., Yang, Z.-L., Levis, S., Sakaguchi, K., Bonan, G. B. and Slater, A. G.:  
772 Parameterization improvements and functional and structural advances in Version 4 of the  
773 Community Land Model, J. Adv. Model. Earth Syst., 3(3), 1–27, doi:10.1029/2011ms000045,  
774 2011.

775 Li, D., Wrzesien, M. L., Durand, M., Adam, J. and Lettenmaier, D. P.: How much runoff  
776 originates as snow in the western United States, and how will that change in the future?,  
777 Geophys. Res. Lett., 44(12), 6163–6172, doi:10.1002/2017GL073551, 2017.

778 Li, D., Lettenmaier, D. P., Margulis, S. A. and Andreadis, K.: The Role of Rain-on-Snow in  
779 Flooding Over the Conterminous United States, Water Resour. Res., 55(11), 8492–8513,  
780 doi:10.1029/2019WR024950, 2019.

781 Liang, X. and Lettenmaier, D.: a simple hydrologically based model of land surface water and



782 energy fluxes for general circulation models, *J. Geophys. ...*, 99 [online] Available from:  
783 <http://onlinelibrary.wiley.com/doi/10.1029/94JD00483/full> (Accessed 16 April 2014), 1994.

784 Livneh, B., Rosenberg, E. A., Lin, C., Nijssen, B., Mishra, V., Andreadis, K. M., Maurer, E. P.  
785 and Lettenmaier, D. P.: A long-term hydrologically based dataset of land surface fluxes and  
786 states for the conterminous United States: Update and extensions, *J. Clim.*, 26(23), 9384–9392,  
787 doi:10.1175/JCLI-D-12-00508.1, 2013.

788 Livneh, B., Bohn, T. J., Pierce, D. W., Munoz-Arriola, F., Nijssen, B., Vose, R., Cayan, D. R.  
789 and Brekke, L.: A spatially comprehensive, hydrometeorological data set for Mexico, the U.S.,  
790 and Southern Canada 1950–2013, *Sci. Data*, 2, 1–12, doi:10.1038/sdata.2015.42, 2015.

791 Di Luzio, M., Johnson, G. L., Daly, C., Eischeid, J. K. and Arnold, J. G.: Constructing  
792 retrospective gridded daily precipitation and temperature datasets for the conterminous United  
793 States, *J. Appl. Meteorol. Climatol.*, 47(2), 475–497, doi:10.1175/2007JAMC1356.1, 2008.

794 Maidment, D. R.: Conceptual Framework for the National Flood Interoperability Experiment,  
795 *JAWRA J. Am. Water Resour. Assoc.*, 53(2), 245–257, doi:10.1111/1752-1688.12474, 2017.

796 Mitchell, J. P., Shrestha, A., Epstein, L., Dahlberg, J. A., Ghezzehei, T., Araya, S., Richter, B.,  
797 Kaur, S., Henry, P., Munk, D. S., Light, S., Bottens, M. and Zaccaria, D.: No-tillage sorghum  
798 and garbanzo yields match or exceed standard tillage yields, *Calif. Agric.*, 112–120,  
799 doi:10.3733/ca.2021a0017, 2022.

800 Nijssen, B., Lettenmaier, D. P., Liang, X., Wetzel, S. W. and Wood, E. F.: Streamflow  
801 simulation for continental-scale river basins and radiative forcings ) applications of the model to  
802 the Columbia and annual flow volumes to within a few percent . Difficulties in reproducing the  
803 Sacramento Model [ Burnash is dominated using an , 33(4), 711–724, 1997.

804 Niu, G. Y., Yang, Z. L., Mitchell, K. E., Chen, F., Ek, M. B., Barlage, M., Kumar, A., Manning,



805 K., Niyogi, D., Rosero, E., Tewari, M. and Xia, Y.: The community Noah land surface model  
806 with multiparameterization options (Noah-MP): 1. Model description and evaluation with local-  
807 scale measurements, *J. Geophys. Res. Atmos.*, 116(12), 1–19, doi:10.1029/2010JD015139, 2011.

808 Norton, C. L., Dannenberg, M. P., Yan, D., Wallace, C. S. A., Rodriguez, J. R., Munson, S. M.,  
809 van Leeuwen, W. J. D. and Smith, W. K.: Climate and Socioeconomic Factors Drive Irrigated  
810 Agriculture Dynamics in the Lower Colorado River Basin, *Remote Sens.*, 13(9), 1659,  
811 doi:10.3390/rs13091659, 2021.

812 Painter, T. H., Rittger, K., McKenzie, C., Slaughter, P., Davis, R. E. and Dozier, J.: Retrieval of  
813 subpixel snow covered area, grain size, and albedo from MODIS, *Remote Sens. Environ.*,  
814 113(4), 868–879, doi:10.1016/j.rse.2009.01.001, 2009.

815 Parajka, J. and Blöschl, G.: Hydrology and Earth System Sciences Validation of MODIS snow  
816 cover images over Austria, *Hydrol. Earth Syst. Sci.*, 10, 679–689 [online] Available from:  
817 [www.hydrol-earth-syst-sci.net/10/679/2006/](http://www.hydrol-earth-syst-sci.net/10/679/2006/), 2006.

818 Rajagopalan, B., Nowak, K., Prairie, J., Hoerling, M., Harding, B., Barsugli, J., Ray, A. and  
819 Udall, B.: Water supply risk on the Colorado River: Can management mitigate?, *Water Resour.*  
820 *Res.*, 45(8), 1–7, doi:10.1029/2008WR007652, 2009.

821 Rajib, A., Evenson, G. R., Golden, H. E. and Lane, C. R.: Hydrologic model predictability  
822 improves with spatially explicit calibration using remotely sensed evapotranspiration and  
823 biophysical parameters, *J. Hydrol.*, 567(April), 668–683, doi:10.1016/j.jhydrol.2018.10.024,  
824 2018.

825 Samimi, M., Mirchi, A., Townsend, N., Gutzler, D., Daggubati, S., Ahn, S., Sheng, Z., Moriasi,  
826 D., Granados-Olivas, A., Alian, S., Mayer, A. and Hargrove, W.: Climate Change Impacts on  
827 Agricultural Water Availability in the Middle Rio Grande Basin, *JAWRA J. Am. Water Resour.*



- 828 Assoc., 58(2), 164–184, doi:10.1111/1752-1688.12988, 2022.
- 829 Senatore, A., Mendicino, G., Gochis, D. J., Yu, W., Yates, D. N. and Kunstmann, H.: Fully  
830 coupled atmosphere-hydrology simulations for the central Mediterranean: Impact of enhanced  
831 hydrological parameterization for short and long time scales, *J. Adv. Model. Earth Syst.*, 7(4),  
832 1693–1715, doi:10.1002/2015MS000510, 2015.
- 833 Shi, L. and Bates, J. J.: Three decades of intersatellite-calibrated High-Resolution Infrared  
834 Radiation Sounder upper tropospheric water vapor, *J. Geophys. Res.*, 116(D4), D04108,  
835 doi:10.1029/2010JD014847, 2011.
- 836 Su, L., Cao, Q., Xiao, M., Mocko, D. M., Barlage, M., Li, D., Peters-Lidard, C. D. and  
837 Lettenmaier, D. P.: Drought Variability over the Conterminous United States for the Past  
838 Century, *J. Hydrometeorol.*, 1153–1168, doi:10.1175/jhm-d-20-0158.1, 2021.
- 839 Tang, Q. and Lettenmaier, D. P.: Use of satellite snow-cover data for streamflow prediction in  
840 the Feather River Basin, California, *Int. J. Remote Sens.*, 31(14), 3745–3762,  
841 doi:10.1080/01431161.2010.483493, 2010.
- 842 Tapley, B. D., Bettadpur, S., Ries, J. C., Thompson, P. F. and Watkins, M. M.: GRACE  
843 Measurements of Mass Variability in the Earth System, *Science* (80-. ), 305(5683), 503–505,  
844 doi:10.1126/science.1099192, 2004.
- 845 Tekeli, A. E., Akyürek, Z., Arda Şorman, A., Şensoy, A. and Ünal Şorman, A.: Using MODIS  
846 snow cover maps in modeling snowmelt runoff process in the eastern part of Turkey, *Remote  
847 Sens. Environ.*, 97(2), 216–230, doi:10.1016/j.rse.2005.03.013, 2005.
- 848 Tobin, K. J. and Bennett, M. E.: Constraining SWAT Calibration with Remotely Sensed  
849 Evapotranspiration Data, *J. Am. Water Resour. Assoc.*, 53(3), 593–604, doi:10.1111/1752-  
850 1688.12516, 2017.



851 Udall, B. and Overpeck, J.: The twenty-first century Colorado River hot drought and  
852 implications for the future, *Water Resour. Res.*, 1–15, doi:10.1002/2016WR019638, 2017.

853 U.S. Bureau of Reclamation: Colorado River Basin Water Supply and Demand Study.  
854 Washington, D.C., 2012.

855 Vano, J. A., Das, T. and Lettenmaier, D. P.: Hydrologic Sensitivities of Colorado River Runoff  
856 to Changes in Precipitation and Temperature\*, *J. Hydrometeorol.*, 13(3), 932–949,  
857 doi:10.1175/JHM-D-11-069.1, 2012.

858 Vano, J. A., Udall, B., Cayan, D. R., Overpeck, J. T., Brekke, L. D., Das, T., Hartmann, H. C.,  
859 Hidalgo, H. G., Hoerling, M., McCabe, G. J., Morino, K., Webb, R. S., Werner, K. and  
860 Lettenmaier, D. P.: Understanding Uncertainties in Future Colorado River Streamflow, *Bull.*  
861 *Am. Meteorol. Soc.*, 95(1), 59–78, doi:10.1175/BAMS-D-12-00228.1, 2014.

862 Wang, Z., Vivoni, E. R., Bohn, T. J. and Wang, Z. H.: A Multiyear Assessment of Irrigation  
863 Cooling Capacity in Agricultural and Urban Settings of Central Arizona, *J. Am. Water Resour.*  
864 *Assoc.*, 57(5), 771–788, doi:10.1111/1752-1688.12920, 2021.

865 Wood, E. F., Roundy, J. K., Troy, T. J., van Beek, L. P. H., Bierkens, M. F. P., Blyth, E., de Roo,  
866 A., Döll, P., Ek, M., Famiglietti, J., Gochis, D., van de Giesen, N., Houser, P., Jaffé, P. R.,  
867 Kollet, S., Lehner, B., Lettenmaier, D. P., Peters-Lidard, C., Sivapalan, M., Sheffield, J., Wade,  
868 A. and Whitehead, P.: Hyperresolution global land surface modeling: Meeting a grand challenge  
869 for monitoring Earth’s terrestrial water, *Water Resour. Res.*, 47(5), doi:10.1029/2010WR010090,  
870 2011.

871 Xiang, T., Vivoni, E. R. and Gochis, D. J.: Seasonal evolution of ecohydrological controls on  
872 land surface temperature over complex terrain, *Water Resour. Res.*, 50(5), 3852–3874,  
873 doi:10.1002/2013WR014787, 2014.



874 Xiang, T., Vivoni, E. R., Gochis, D. J. and Mascaro, G.: On the diurnal cycle of surface energy  
875 fluxes in the North American monsoon region using the WRF-Hydro modeling system, J.  
876 Geophys. Res. Atmos., 122(17), 9024–9049, doi:10.1002/2017JD026472, 2017.

877 Xiao, M., Udall, B. and Lettenmaier, D. P.: On the causes of declining Colorado River  
878 streamflows, Water Resour. Res., 2, 1–18, doi:10.1029/2018WR023153, 2018.

879 Yun, X., Tang, Q., Wang, J., Liu, X., Zhang, Y., Lu, H., Wang, Y., Zhang, L. and Chen, D.:  
880 Impacts of climate change and reservoir operation on streamflow and flood characteristics in the  
881 Lancang-Mekong River Basin, J. Hydrol., 590(June), 125472,  
882 doi:10.1016/j.jhydrol.2020.125472, 2020.

883 Zhang, Y., You, Q., Chen, C. and Li, X.: Flash droughts in a typical humid and subtropical  
884 basin: A case study in the Gan River Basin, China, J. Hydrol., 551, 162–176,  
885 doi:10.1016/j.jhydrol.2017.05.044, 2017.

886 Zhengming Wan and Dozier, J.: A generalized split-window algorithm for retrieving land-  
887 surface temperature from space, IEEE Trans. Geosci. Remote Sens., 34(4), 892–905,  
888 doi:10.1109/36.508406, 1996.

889 Zhou, Q., Yang, S., Zhao, C., Cai, M., Lou, H., Luo, Y. and Hou, L.: Development and  
890 implementation of a spatial unit non-overlapping water stress index for water scarcity evaluation  
891 with a moderate spatial resolution, Ecol. Indic., 69, 422–433, doi:10.1016/j.ecolind.2016.05.006,  
892 2016.

893 Zink, M., Mai, J., Cuntz, M. and Samaniego, L.: Conditioning a Hydrologic Model Using  
894 Patterns of Remotely Sensed Land Surface Temperature, Water Resour. Res., 54(4), 2976–2998,  
895 doi:10.1002/2017WR021346, 2018.

896